

Study of a droplet breakup process in decaying homogeneous isotropic turbulence based on the phase-field DUGKS approach

Jun Lai,^{1,2} Tao Chen,² Shengqi Zhang,¹ Zuoli Xiao,¹ Shiyi Chen,^{1,2,3} and Lian-Ping Wang^{2,3, a)}

¹⁾*State Key Laboratory for Turbulence and Complex Systems,
College of engineering, Peking University, Beijing 100871,
P.R. China*

²⁾*Guangdong Provincial Key Laboratory of Turbulence Research and Applications,
Center for Complex Flows and Soft Matter Research and Department of Mechanics
and Aerospace Engineering, Southern University of Science and Technology,
Shenzhen 518055, P.R. China*

³⁾*Guangdong-Hong Kong-Macao Joint Laboratory for Data-Driven Fluid Mechanics
and Engineering Applications, Southern University of Science and Technology,
Shenzhen 518055, China*

(Dated: 24 June 2022)

Abstract

The breakup of a spherical droplet in a decaying homogeneous isotropic turbulence is studied by solving the Cahn-Hilliard-Navier-Stokes equations, using the discrete unified gas kinetic scheme combined with the free-energy-based phase-field model. We focus on the combined effects of turbulence and surface tension on the breakup process by assuming that the two fluid phases have the same density and same viscosity. The key physical parameters of the system include the volume fraction ($\phi = 6.54\%$), the initial Weber number ($We = 21.7$), and the initial Taylor microscale Reynolds number ($Re_\lambda = 58$). Due to the turbulence decay, the Weber number decreases monotonically in time to a value of less than 0.01, providing a great opportunity to study the competing effects of turbulent kinetic energy and interfacial free energy on the dynamics of the two-phase system. Three distinct stages of droplet evolution are identified, namely, the deformation stage when the initially spherical droplet evolves into an irregular geometric shape with complex structures, the breakup stage when many daughter droplets are formed, and the restoration stage when the droplets relax towards spherical shape. These three stages are analyzed systematically from several perspectives: (1) a geometric perspective concerning the maximum equivalent diameter, the total number of droplets, total interface area, and probability distribution of droplet diameters, (2) a dynamic perspective concerning the evolution of local velocity and vorticity at the fluid-fluid interface, (3) a global perspective concerning the evolution of average kinetic energy / dissipation rate and their Fourier spectra, (4) spherical harmonics based energetics concerning simultaneous transfer of kinetic energy across different length scales and different radii relative to initial droplet center, and (5) the time evolution of global kinetic energy and free energy of the system. It is found that the ending time of the breakup stage can be estimated by the Hinze criterion. The kinetic energy of the two-phase flow during the breakup stage is found to have a power-law decay with an exponent -1.76 , compared to the exponent (-1.65) for the single-phase flow during the same time period, mainly due to the enhanced viscous dissipation generated by the daughter droplets. Energy spectra of the two-phase flow show power-law decay, with a slope between -4 and -3 , at high wave numbers, both in the usual Fourier spectral space and in the spherical harmonics space.

Keywords: turbulence-interface interaction, droplet breakup, DUGKS, phase-field, energy

^{a)}Electronic mail: wanglp@sustech.edu.cn

I. INTRODUCTION

Liquid-liquid or gas-liquid two-phase turbulent flows appear in many natural processes and engineering applications, such as wind-cloud interaction, rain formation, air-sea interaction, spray combustion, hydrocarbon separation, emulsion polymerization, fire extinction, irrigation, *etc.* Understanding the evolution and properties of two-phase flows is therefore of major technological and scientific interest.¹ These flows could be governed by a number of parameters including density ratio, viscosity ratio, volume fraction, Weber number We (the ratio of inertial force to surface tension force), and Reynolds number Re (the ratio of inertial force to viscous force). The interaction between the evolving interface topology and the turbulent flow is the most important and difficult issue in these flows.

With the advances in computer science and numerical methods, direct numerical simulation (DNS) has been developed to address the dynamics of two-phase turbulent flows at the interface scale.^{2–9} There are different ways of classifying these flows.^{4,10} By virtue of the properties of dispersed phase, they can be classified into droplet-^{5,11,12} and bubble-laden^{7,8,13} flows, mainly depending on the density of dispersed phase compared to the continuous phase. The dispersed phase can be classified into non-deformable droplets/bubbles (*e.g.*, the point-particle model)^{14–16} or deformable droplets/bubbles^{7,12,17}, depending on the deformability of the dispersed phase. The two-phase turbulent flows studied in DNS so far include mostly decaying homogeneous isotropic turbulence (DHIT),^{11,13} forced homogeneous isotropic turbulence (FHIT),^{3,8,18} and turbulent channel flows.^{2,7,12,19}

Interface-resolved DNS methods are divided into macroscopic methods and mesoscopic methods.^{20,21} The macroscopic methods solving the continuum mechanics equations include the front-tracking method,²² volume-of-fluid (VOF) method,^{23,24} level-set method,^{24,25} *etc.* These are the traditional multiphase computational fluid dynamics (CFD) methods. It remains challenging for the front-tracking method to model interface breakup and coalescence, because the interface needs to be artificially ruptured.^{20,22} For the VOF and level-set methods, an interface reconstruction step is required, which would be a complex task to implement.^{20,23}

The mesoscopic approaches are formulated based on properly-designed model Boltzmann equations. The widely used mesoscopic approaches, developed mainly over the past 30 years, include the color-gradient model,²⁶ pseudo-potential model,^{27,28} free-energy model,²⁹ *etc.* Gunstensen *et al.* (1991)²⁶ developed the first multicomponent lattice Boltzmann method,³⁰ which is

usually called color-gradient model or color-fluid model nowadays. The perturbation step in this model would cause an anisotropic surface tension that induces unphysical velocity and vorticity near the fluid-fluid interface.^{20,30} Shan & Chen (1993)²⁷ presented a pseudo-potential model, known as the Shan-Chen model, which can separate fluid phases or components automatically and improve the isotropy of the surface tension as well,³⁰ while the spurious velocity is typically observed near the interface.²⁰ Swift *et al.* (1996)²⁹ proposed the free-energy model. Compared to the previous models, the free-energy-based phase-field model is thermodynamically consistent,^{20,30} which serves the physical basis for the simulations in this paper. It is noted that the phase field equations can also be solved directly using the traditional CFD methods.³¹

In recent years, homogeneous isotropic turbulence (HIT) laden with deformable droplets is an active research area. For droplets evolution in a forced HIT (FHIT), Derksen & Akker (2007)¹⁸ have reported one of the first DNS results on liquid-liquid dispersions. Using a lattice Boltzmann method (LBM), *i.e.*, the He-Chen-Zhang (HCZ) model,³² they found that the droplets increased the turbulence energy at small scales because of the generation of small-scale turbulence in the continuous phase. Perlekar *et al.* (2012)³³ studied the droplet size distribution in FHIT based on the multicomponent Shan-Chen LBM. They found that the droplet emulsion can be maintained for a long time, and, for the small volume fraction case, the average droplet diameter is in agreement with the Hinze criterion.³⁴ Komrakova *et al.* (2015)³⁵ simulated liquid-liquid dispersions in FHIT based on the phase-field model combined with LBM. They observed that it is impossible to form a dispersion if the volume fraction of the initial droplet is higher than 0.05, because a large portion of dispersed phase would remain connected. Albernaz *et al.* (2017)³ used pseudo-potential LBM with the multi-relaxation time (MRT) collision operator, to study the heat transfer of droplets in FHIT. They found that temperature fluctuations, surface tension variation and turbulence intensity influence the occurrence of evaporation and condensation. Shao *et al.* (2018)³⁶ used the level-set method to study the effects of the Weber number on a droplet breakup in FHIT. They found that the initial spherical droplet tended to break down into small droplets with increasing Weber number. Furthermore, at the statistically stationary state, the local topology of the bi-axial strain is suppressed inside the droplet region compared to the outside carrier-phase. Mukherjee *et al.* (2019)⁵ studied droplet-turbulence interactions and quasi-equilibrium dynamics in FHIT, based on the pseudo-potential LBM. They observed that droplet breakup extracts the kinetic energy from the large scales and injects into the small scales, and turbulent emulsions would evolve into a quasi-equilibrium cycle of alternating coalescence and breakup dominated processes.

While FHIT produces a statistically stationary flow field which is beneficial for studying droplet size distribution,^{4,5,18,33,35} the artificial large-scale forcing term in FHIT could contaminate the two-way coupling interactions,^{4,10} especially when the energy transfer across scales is analyzed. Therefore, in this study we choose DHIT as the background flow field. To our knowledge, only Dodd & Ferrante (2016)¹¹ and Dodd & Jofre (2019)³⁷ studied droplets evolution in DHIT. To explain the basic mechanisms of droplet-turbulence interaction, Dodd & Ferrante (2016)¹¹ simulated motion of droplets of the Taylor length scale size in DHIT based on VOF, and studied the energy transfer and viscous dissipation during the flow evolution. They showed that the coalescence process would increase the turbulence kinetic energy (TKE) and the breakup process would decrease the TKE. Dodd & Jofre (2019)³⁷ further showed that, increasing the droplet Weber number would decrease the interfacial shear stress and viscous length scale at the droplet surface, while increasing the density and viscosity ratio would increase the interfacial shear stress. The breakup process of a droplet in a DHIT field has not been carefully studied with DNS.

In this paper, we explore the capabilities of a mesoscopic method based on the Boltzmann equation, coupled with the phase-field model, to simulate the breakup of a large droplet in a complex background flow field. A relatively new gas kinetic scheme known as the discrete unified gas kinetic scheme (DUGKS)^{38,39} is adopted here. DUGKS combines the advantages of the LBM^{30,40} and unified gas kinetic scheme (UGKS).⁴¹ In DUGKS, a model Boltzmann equation is solved using an accurate finite-volume formulation coupling tightly the kinetic particle transport and particle collisions. Compared to LBM, DUGKS can more easily incorporate irregular meshes and different kinetic particle velocity models. The scheme has been applied to simulate single-phase HIT⁴² and wall bounded turbulent flows.⁴³ The first objective of this paper is to incorporate the phase-field transport equation with the DUGKS framework, in order to simulate three-dimensional immiscible two-phase turbulent flows. This extends the capabilities of DUGKS. Specifically, as a first step we consider the breakup process of a spherical droplet in a turbulent background flow.

Another objective of this study is to carefully investigate the evolution of droplet interfaces in DHIT. Droplet breakup in a turbulent flow is a complex physical phenomenon mainly controlled by the competition between the kinetic energy and the interface free energy. The kinetic energy makes the droplet deform and break up, increasing the overall interface area. The free energy tends to drive droplet coalescence and make the droplets more spherical. Three distinct stages of evolution will be shown: (1) the deformation stage, where the initially spherical droplet evolves into an irregular geometric pattern with complex structures, (2) the breakup stage, during which

many small droplets are generated from the large droplet, (3) the restoration stage, during which all the droplets return to spherical and may coalesce with other nearby droplets, eventually reaching a quasi-stationary state.

The rest of the paper is organized as follows. In Section II, the simulation methodology is introduced, including both the mesoscopic and macroscopic descriptions of the system, and DUGKS. In Section III, a stationary droplet is simulated first to test our code. In Section IV, a freely-deforming droplet in decaying turbulent flow is simulated, and is compared to a single-phase flow with the same initial velocity field. In Section V, the breakup process of a large spherical droplet in DHIT is displayed in detail, and the three evolution stages, *i.e.*, the deformation stage, breakup stage, restoration stage, are revealed and analyzed. Main conclusions are presented in Section VI. The appendices cover the inverse design of the Boltzmann equations for the Cahn-Hilliard-Navier-Stokes (CHNS) system, an algorithm for isolating and computing the volume of individual droplets, and theoretical results concerning the kinetic energy of two-phase flow in the spectra space.

II. METHODOLOGY

A. Phase-field model and macroscopic equations

The phase-field model is a well-known diffuse-interface (DI) method for solving interfacial flow problems.^{44–49} In the phase-field model, the free energy of two-phase flow is^{29,50–53}

$$F(\phi) = \int_V \left[\psi(\phi) + \frac{\kappa}{2} |\nabla \phi|^2 \right] dV, \quad (1)$$

with a double-well form for $\psi(\phi)$,

$$\psi(\phi) = \beta (\phi - \phi_A)^2 (\phi - \phi_B)^2. \quad (2)$$

Here ϕ is an order parameter to distinguish different phases, ϕ_A and ϕ_B are phase parameters corresponding to the two phases. In this paper, $\phi_A = 1$ and $\phi_B = 0$. V is the volume of the system. $\psi(\phi)$ is the bulk free-energy density acting as a *phobic* effect, which represents separation of the two phases into the bulk region. $\kappa |\nabla \phi|^2 / 2$ is the interfacial free-energy density acting as a *philic* effect, which prefers mixing with each other. ∇ is the gradient operator. The parameters κ and β

are related to the interfacial surface tension σ and the interfacial thickness parameter W as

$$\sigma = \frac{|\phi_A - \phi_B|^3}{6} \sqrt{2\kappa\beta}, \quad W = \frac{1}{\phi_A - \phi_B} \sqrt{\frac{8\kappa}{\beta}}. \quad (3)$$

It is clear that $W \sim \sqrt{\kappa/\beta}$. Therefore, if κ becomes larger (interfacial free-energy is larger) or β becomes smaller (bulk free-energy is smaller), then W becomes larger, as expected. The variation of the free energy with respect to ϕ yields the chemical potential μ_ϕ , *i.e.*,

$$\begin{aligned} \mu_\phi &= \frac{\delta F}{\delta \phi} \\ &= 4\beta (\phi - \phi_A) (\phi - \phi_B) \left(\phi - \frac{\phi_A + \phi_B}{2} \right) - \kappa \nabla^2 \phi. \end{aligned} \quad (4)$$

For a flat surface at equilibrium, $\mu_\phi = 0$, leading to^{46,52}

$$\phi(x) = \frac{\phi_A + \phi_B}{2} + \frac{\phi_A - \phi_B}{2} \tanh\left(\frac{2x}{W}\right), \quad (5)$$

where x is the signed distance normal to the interface.

The macroscopic governing equations contain three parts, *i.e.*, the continuity equation, the momentum equation, and the Cahn-Hilliard (CH) equation,^{54,55} which can maintain the local mass conservation and energy decay properties in theory.^{56,57}

$$\frac{1}{\rho RT} \frac{\partial p}{\partial t} + \nabla \cdot \mathbf{u} = -\gamma \nabla \cdot (M_{CH} \nabla \mu_\phi), \quad (6a)$$

$$\frac{\partial(\rho \mathbf{u})}{\partial t} + \nabla \cdot (\rho \mathbf{u} \mathbf{u}) = -\nabla p + \nabla \cdot [\mu (\nabla \mathbf{u} + \mathbf{u} \nabla)] + \mathbf{F}, \quad (6b)$$

$$\frac{\partial \phi}{\partial t} + \nabla \cdot (\phi \mathbf{u}) = \nabla \cdot (M_{CH} \nabla \mu_\phi), \quad (6c)$$

with fluid density ρ and dynamic viscosity μ given by linear models³² as

$$\rho = \frac{\phi - \phi_B}{\phi_A - \phi_B} \rho_A + \frac{\phi - \phi_A}{\phi_B - \phi_A} \rho_B, \quad (7a)$$

$$\mu = \frac{\phi - \phi_B}{\phi_A - \phi_B} \mu_A + \frac{\phi - \phi_A}{\phi_B - \phi_A} \mu_B, \quad (7b)$$

where R is the gas constant, T is the reference temperature, \mathbf{u} is the fluid velocity, p is the pressure, t is the time. $\gamma = (\rho_A - \rho_B) / (\phi_A \rho_B - \phi_B \rho_A)$ is a constant related to the two-phase order parameters and densities. The mobility M_{CH} is assumed to be a constant. $\mathbf{F} = -\phi \nabla \mu_\phi$ is the interfacial force. ρ_A , ρ_B and μ_A , μ_B are the densities and the dynamic viscosities of the two phases. The above macroscopic system is known as the Cahn-Hilliard-Navier-Stokes (CHNS) system.

It is noted that in the incompressible formulation, the density field ρ is solely determined by the phase field ϕ , which is independent of the pressure p . The usual divergence-free velocity ($\nabla \cdot \mathbf{u} = 0$) is first modified by adding a term $-\gamma \nabla \cdot (M_{CH} \nabla \mu_\phi)$ to the right hand side to ensure that the local mass conservation is satisfied even in the interfacial regions.⁴⁵ Furthermore, the first term on the left hand side of Eq. (6a) is added to facilitate the design of the model LB equation (see Appendix A), which essentially amounts to the artificial compressibility solver.⁵⁸

B. The mesoscopic model

The double-distribution function model is used to recover the hydrodynamic equations and CH equation. The following two model Boltzmann equations with Bhatnager-Gross-Krook (BGK) collision model⁵⁹ are employed^{45,46}

$$\frac{\partial f_\alpha}{\partial t} + \xi_\alpha \cdot \nabla f_\alpha = -\frac{f_\alpha - f_\alpha^{eq}}{\tau_f} + S_\alpha^f, \quad (8a)$$

$$\frac{\partial g_\alpha}{\partial t} + \xi_\alpha \cdot \nabla g_\alpha = -\frac{g_\alpha - g_\alpha^{eq}}{\tau_g} + S_\alpha^g, \quad (8b)$$

where the pressure/velocity distribution function $f_\alpha = f_\alpha(\mathbf{x}, t)$ and the order-parameter distribution function $g_\alpha = g_\alpha(\mathbf{x}, t)$ corresponding to a discrete particle velocity ξ_α are functions of position \mathbf{x} and time t . τ_f and τ_g are the relaxation times. The key to recover the macroscopic governing equations is to properly design the two equilibrium distribution functions ($f_\alpha^{eq}, g_\alpha^{eq}$) and the two source terms (S_α^f, S_α^g). The macroscopic variables are obtained through the moments of the distribution functions,

$$\phi(\mathbf{x}, t) = \sum_{\alpha=0}^{Q-1} g_\alpha(\mathbf{x}, t), \quad (9a)$$

$$\mathbf{u}(\mathbf{x}, t) = \frac{1}{\rho(\mathbf{x}, t) RT} \sum_{\alpha=0}^{Q-1} f_\alpha(\mathbf{x}, t) \xi_\alpha, \quad (9b)$$

$$p(\mathbf{x}, t) = \sum_{\alpha=0}^{Q-1} f_\alpha(\mathbf{x}, t), \quad (9c)$$

where Q is the number of the discrete velocities in the particle velocity model. In this study, the D3Q19 discrete-velocity model ($Q = 19$) is used, with

$$\frac{\xi_\alpha}{c} = \begin{cases} (0, 0, 0), & \alpha = 0, \\ (\pm 1, 0, 0), (0, \pm 1, 0), (0, 0, \pm 1), & \alpha = 1 - 6, \\ (0, \pm 1, \pm 1), (\pm 1, 0, \pm 1), (\pm 1, \pm 1, 0), & \alpha = 7 - 18, \end{cases} \quad (10)$$

where $c = \sqrt{3RT} = 1$ in the lattice units. The weighting coefficients are $\omega_0 = 1/3$, $\omega_{1-6} = 1/18$, $\omega_{7-18} = 1/36$. Following Zhang *et al.* (2018)⁴⁵'s work, the equilibrium distribution functions are

$$f_\alpha^{eq} = \omega_\alpha p + s_\alpha RT \rho, \quad (11a)$$

$$g_\alpha^{eq} = \begin{cases} (s_0 + 1)\phi + (\omega_0 - 1)\eta\mu_\phi, & \alpha = 0, \\ s_\alpha\phi + \omega_\alpha\eta\mu_\phi, & \alpha \neq 0, \end{cases} \quad (11b)$$

where

$$s_\alpha = \omega_\alpha \left[\frac{\boldsymbol{\xi}_\alpha \cdot \mathbf{u}}{RT} + \frac{(\boldsymbol{\xi}_\alpha \cdot \mathbf{u})^2}{2(RT)^2} - \frac{u^2}{2RT} \right]. \quad (12)$$

η is an adjustable constant used to improve numerical stability. $\eta = 1$ in our simulations.

The source terms are designed to take the following forms⁴⁵

$$S_\alpha^f = (\boldsymbol{\xi}_\alpha - \mathbf{u}) \cdot [(\omega_\alpha + s_\alpha) \mathbf{F} + s_\alpha RT \nabla \rho] - \omega_\alpha \gamma RT \rho \nabla \cdot (M_{CH} \nabla \mu_\phi), \quad (13a)$$

$$S_\alpha^g = (\omega_\alpha + s_\alpha) \frac{\phi}{RT \rho} (\boldsymbol{\xi}_\alpha - \mathbf{u}) \cdot (\mathbf{F} - \nabla p). \quad (13b)$$

Here the two relaxation times are

$$\tau_f = \frac{\mu}{\rho RT}, \quad \tau_g = \frac{M_{CH}}{\eta RT}. \quad (14)$$

This can be shown by applying the Chapman-Enskog analysis.^{45,60} It is noted that the design of equilibrium distribution functions and source terms is not unique. They are applied to recover the macroscopic governing equations, Eqs. (6a-c). Essentially, they are constrained by a few moment-integral conditions, which are derived systematically in Appendix A.

When the density is constant in the whole flow field (*i.e.*, $\rho_A = \rho_B$), the source term S_α^f is then simplified to

$$S_\alpha^f = (\boldsymbol{\xi}_\alpha - \mathbf{u}) \cdot (\omega_\alpha + s_\alpha) \mathbf{F}. \quad (15)$$

C. The numerical algorithm: discrete unified gas kinetic scheme (DUGKS)

The DUGKS approach is briefly summarized here. More details can be found in Guo *et al.*^{38,39} Eqs. (8) can be written in an unified form,

$$\frac{\partial \varphi_\alpha}{\partial t} + \boldsymbol{\xi}_\alpha \cdot \nabla \varphi_\alpha = \Omega_\alpha^\varphi + S_\alpha^\varphi, \quad (16)$$

where $\varphi = f$ or g represents the distribution function, and $\Omega_\alpha^\varphi = -(\varphi_\alpha - \varphi_\alpha^{eq})/\tau_\varphi$ is the corresponding collision term.

DUGKS is a finite-volume scheme. The computational domain is divided into a set of control volumes. Integrating Eq. (16) over a control volume V_j centered at \mathbf{x}_j from t_n to t_{n+1} , with the midpoint rule for the advection term and trapezoidal rule for Ω and S , yields

$$\begin{aligned} & \varphi_\alpha^{n+1} - \varphi_\alpha^n + \frac{\delta t}{|V_j|} J_\alpha^{n+1/2} \\ &= \frac{\delta t}{2} \left(\Omega_\alpha^{\varphi, n+1} + \Omega_\alpha^{\varphi, n} \right) + \frac{\delta t}{2} \left(S_\alpha^{\varphi, n+1} + S_\alpha^{\varphi, n} \right), \end{aligned} \quad (17)$$

with

$$\varphi_\alpha^n = \frac{1}{|V_j|} \int_{V_j} \varphi_\alpha(\mathbf{x}, t_n) dV, \quad (18a)$$

$$J_\alpha^{n+1/2} = \int_{\partial V_j} (\boldsymbol{\xi}_\alpha \cdot \mathbf{n}) \varphi_\alpha(\mathbf{x}, t_{n+1/2}) dA, \quad (18b)$$

$$\Omega_\alpha^{\varphi, n} = \frac{1}{|V_j|} \int_{V_j} \Omega_\alpha^\varphi(\mathbf{x}_j, t_n) dV, \quad (18c)$$

$$S_\alpha^{\varphi, n} = \frac{1}{|V_j|} \int_{V_j} S_\alpha^\varphi(\mathbf{x}_j, t_n) dV, \quad (18d)$$

where $|V_j|$ and ∂V_j are the volume and surface of the grid cell V_j . Introducing linear transformations

$$\begin{aligned} \tilde{\varphi}_\alpha &= \varphi_\alpha - \frac{\delta t}{2} (\Omega_\alpha^\varphi + S_\alpha^\varphi) \\ &= \frac{2\tau_\varphi + \delta t}{2\tau_\varphi} \varphi_\alpha - \frac{\delta t}{2\tau_\varphi} \varphi_\alpha^{eq} - \frac{\delta t}{2} S_\alpha^\varphi, \end{aligned} \quad (19a)$$

$$\begin{aligned} \tilde{\varphi}_\alpha^+ &= \varphi_\alpha + \frac{\delta t}{2} (\Omega_\alpha^\varphi + S_\alpha^\varphi) \\ &= \frac{2\tau_\varphi - \delta t}{2\tau_\varphi + \delta t} \tilde{\varphi}_\alpha + \frac{2\delta t}{2\tau_\varphi + \delta t} \varphi_\alpha^{eq} + \frac{2\tau_\varphi \delta t}{2\tau_\varphi + \delta t} S_\alpha^\varphi, \end{aligned} \quad (19b)$$

then Eq. (17) can be written as

$$\tilde{\varphi}_\alpha^{n+1} = \tilde{\varphi}_\alpha^{+, n} - \frac{\delta t}{|V_j|} J_\alpha^{n+1/2}, \quad (20)$$

namely, the implicitness in the collision term and source term are removed.

To update $\tilde{\varphi}_\alpha^{n+1}$, the key now is the evaluation of the flux across the cell interface at half time step $t_{n+1/2}$. Integrating Eq. (16) for a half time step $h = \delta t/2$ along the characteristic line, yields

$$\begin{aligned} & \varphi_\alpha(\mathbf{x}_b, t_n + h) - \varphi_\alpha(\mathbf{x}_b - \boldsymbol{\xi}_\alpha h, t_n) \\ &= \frac{h}{2} \left[\Omega_\alpha^\varphi(\mathbf{x}_b, t_n + h) + \Omega_\alpha^\varphi(\mathbf{x}_b - \boldsymbol{\xi}_\alpha h, t_n) \right] \\ &+ \frac{h}{2} \left[S_\alpha^\varphi(\mathbf{x}_b, t_n + h) + S_\alpha^\varphi(\mathbf{x}_b - \boldsymbol{\xi}_\alpha h, t_n) \right], \end{aligned} \quad (21)$$

where the interface location $\mathbf{x}_b = (\mathbf{x}_j + \mathbf{x}_{j+1})/2$ for the uniform grid. Similarly, by introducing the linear transformations

$$\bar{\varphi}_\alpha = \frac{2\tau_\varphi + h}{2\tau_\varphi} \varphi_\alpha - \frac{h}{2\tau_\varphi} \varphi_\alpha^{eq} - \frac{h}{2} S_\alpha^\varphi, \quad (22a)$$

$$\bar{\varphi}_\alpha^+ = \frac{2\tau_\varphi - h}{2\tau_\varphi + h} \bar{\varphi}_\alpha + \frac{2h}{2\tau_\varphi + h} \varphi_\alpha^{eq} + \frac{2\tau_\varphi h}{2\tau_\varphi + h} S_\alpha^\varphi, \quad (22b)$$

Eq. (21) can be reduced in an explicit form as

$$\bar{\varphi}_\alpha(\mathbf{x}_b, t_n + h) = \bar{\varphi}_\alpha^+(\mathbf{x}_b - \boldsymbol{\xi}_\alpha h, t_n). \quad (23)$$

The right hand side of Eq. (23) can be approximated using the first-order Taylor expansion,

$$\bar{\varphi}_\alpha^+(\mathbf{x}_b - \boldsymbol{\xi}_\alpha h, t_n) \approx \bar{\varphi}_\alpha^+(\mathbf{x}_b, t_n) - \boldsymbol{\xi}_\alpha h \cdot \boldsymbol{\sigma}_b, \quad (24)$$

where $\boldsymbol{\sigma}_b = \nabla \bar{\varphi}_\alpha^+(\mathbf{x}_b, t_n)$.

Inverting the transformation, Eq. (22a), the original distribution $\varphi_\alpha(\mathbf{x}_b, t_n + h)$ is

$$\varphi_\alpha = \frac{2\tau_\varphi}{2\tau_\varphi + h} \bar{\varphi}_\alpha + \frac{h}{2\tau_\varphi + h} \varphi_\alpha^{eq} + \frac{\tau_\varphi h}{2\tau_\varphi + h} S_\alpha^\varphi, \quad (25)$$

which can now be used to evaluate $\mathbf{J}_\alpha^{n+1/2}$ in Eq. (18b).

All the transformations are linear and only two of the distributions are independent. It is straightforward to show that

$$\tilde{\varphi}_\alpha^+ = \frac{4}{3} \bar{\varphi}_\alpha^+ - \frac{1}{3} \tilde{\varphi}_\alpha, \quad (26)$$

$$\bar{\varphi}_\alpha^+ = \frac{2\tau_\varphi - h}{2\tau_\varphi + \delta t} \tilde{\varphi}_\alpha + \frac{3h}{2\tau_\varphi + \delta t} \varphi_\alpha^{eq} + \frac{3\tau_\varphi h}{2\tau_\varphi + \delta t} S_\alpha^\varphi. \quad (27)$$

Finally, $\tilde{\varphi}_\alpha^{n+1}$ can be obtained from Eq. (20).

In the code, we track \tilde{g}_α and \tilde{f}_α , then the macroscopic variables are evaluated as^{45,46}

$$\phi(\mathbf{x}_j, t_n + \delta t) = \sum_{\alpha=0}^{Q-1} \tilde{g}_\alpha, \quad (28a)$$

$$\mathbf{u}(\mathbf{x}_j, t_n + \delta t) = \frac{1}{RT\rho} \left(\sum_{\alpha=0}^{Q-1} \boldsymbol{\xi}_\alpha \tilde{f}_\alpha + \frac{\delta t}{2} \mathbf{F} \right), \quad (28b)$$

$$p(\mathbf{x}_j, t_n + \delta t) = \sum_{\alpha=0}^{Q-1} \tilde{f}_\alpha + \frac{\delta t}{2} RT [\mathbf{u} \cdot \nabla \rho - \gamma \rho \nabla \cdot (M_{CH} \nabla \mu_\phi)]. \quad (28c)$$

For the special case of $\rho_A = \rho_B$, Eq. (28c) can be simplified to

$$p(\mathbf{x}_j, t_n + \delta t) = \sum_{\alpha=0}^{Q-1} \tilde{f}_\alpha. \quad (29)$$

The time step size is determined by the Courant-Friedrichs-Lewy (CFL) condition^{38,41,45,46,61}

$$\delta t = CFL \frac{\delta x_{\min}}{c + |\mathbf{u}|_{\max}}, \quad (30)$$

where δx_{\min} and $|\mathbf{u}|_{\max}$ represent the minimal grid spacing and maximum hydrodynamic velocity magnitude, respectively, CFL denotes the CFL number.

Another detail is that there are first-order and second-order spatial derivatives involved in the phase-field DUGKS (PF-DUGKS) approach. These are evaluated by second-order central finite difference schemes.

III. A STATIONARY DROPLET

We first simulate a stationary droplet to validate our code based on the PF-DUGKS approach. All the parameters are in lattice units in this paper unless otherwise stated. Initially, a spherical droplet with a radius $R_0 = 32.0$ is placed at the center of the computational domain of size 128^3 . The periodic boundary conditions are applied to all spatial directions. The density ratio and viscosity ratio are both one. As reported by Zu & He (2013)⁶² and Chen *et al.* (2019),⁴⁶ a small mobility may cause numerical instability, while a larger mobility would increase the parasitic currents. As a compromise, $M_{CH} = 0.01$ is chosen. $W = 3.0$, implies the Cahn number $Ch = W/R_0 = 0.0938$. The other parameters are $\tau_f = \tau_g = 0.5$, $\sigma = 8.0 \times 10^{-4}$, $CFL = 0.25$. The order parameter is initialized as^{45,46,62,63}

$$\phi(r_D) = \frac{\phi_A + \phi_B}{2} + \frac{\phi_A - \phi_B}{2} \tanh\left(2 \frac{R_0 - r_D}{W}\right), \quad (31)$$

where $D = 2, 3$ for 2D and 3D cases, respectively. The distance between any point $((x, y)$ or $(x, y, z))$ and the droplet center $((x_c, y_c)$ or $(x_c, y_c, z_c))$ are $r_2 = \sqrt{(x - x_c)^2 + (y - y_c)^2}$, $r_3 = \sqrt{(x - x_c)^2 + (y - y_c)^2 + (z - z_c)^2}$ for 2D and 3D. The initial velocity and hydrodynamic pressure are both set to zero in the whole domain. In this case, the dimensionless time is defined as $t^* = \frac{t}{R_0} \sqrt{\frac{\sigma}{\rho R_0}}$.

The order parameter as a function of the distance from the droplet center at different times are showed in Fig. 1. We observe that the distribution of the order parameter ϕ is nearly stable for a

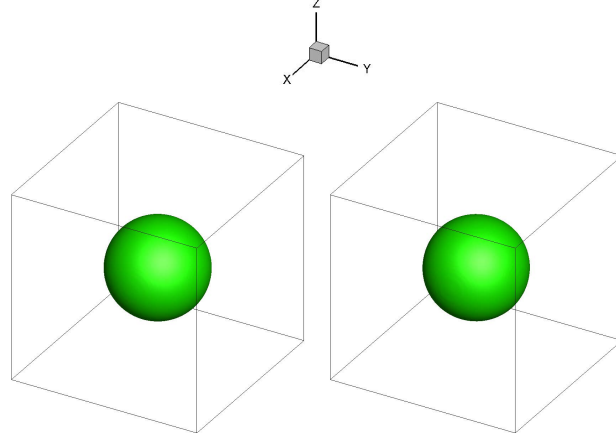
TABLE I. Maximum and minimum of each term in x direction of momentum equation

	$\left\{ \frac{\partial(\rho u)}{\partial t} \right\}_x$	$\{\nabla \cdot (\rho \mathbf{u} \mathbf{u})\}_x$	$\{-\nabla p\}_x$	$\{\nabla \cdot (\mu \nabla \mathbf{u})\}_x$	$\{\nabla \cdot (\mu \mathbf{u} \nabla)\}_x$	$\{-\phi \nabla \mu_\phi\}_x$
max	4.5727e-12	4.5970e-11	1.3882e-05	3.1267e-06	8.2250e-07	1.4410e-05
min	-4.5727e-12	-4.5970e-11	-1.3882e-05	-3.1267e-06	-8.2250e-07	-1.4410e-05

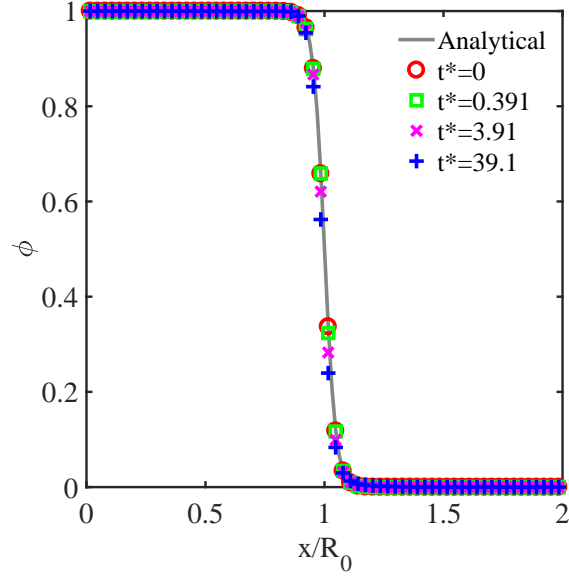
long time and the interface between the two phases remains unaltered. For a fixed position near the interface, ϕ decreases slightly, which indicates that the droplet becomes slightly smaller over time because of the minor mass loss.^{56,64–66} At $t^* = 39.1$, *i.e.*, after 1×10^6 time steps, the volume $V(t^* = 39.1)$ is found to be $0.990V(t^* = 0)$, while it is $0.995V(t^* = 0)$ for the 2D case with the same simulation parameters. In terms of the radius ratio, we have $R(t^* = 39.1)/R(t^* = 0) = 0.997$ and 0.998 for the 3D and 2D cases, respectively, which means that the droplet size in 3D case decreases slightly faster than that in the 2D case. The observed values of $R(t^*)/R(t^* = 0)$ are similar as that reported by Lee & Fischer (2006)⁶⁷ and Zu & He (2013).⁶²

Then we examine the momentum equation, Eq. (6b), along the same centerline in the x direction at $t^* = 39.1$. We calculate all the terms in the x direction of Eq. (6b), the maximum and minimum values are presented in Table I. From this table, we observe that the sum of maximum and minimum is always zero for each of these six terms, because of the symmetry of the problem with respect to the center of the droplet, or equivalently asymmetry in Cartesian coordinates. Furthermore, the time derivative term and the advection term can be neglected. The viscous term, which is separated into two parts in the table, is also small compared to the pressure gradient term and the interfacial force term. In Fig. 2, we can observe that the pressure gradient term is well balanced by the interfacial force term in the bulk region. In the interface region, they also balance each other but not precisely. If we add the viscous term, the balance in the interface region is closely met. In summary, the pressure gradient term and the interfacial force term roughly balance each other, and the viscous term makes a noticeable contribution near the interface region only. Very similar results were shown in Chen *et al.* (2019).⁴⁶

Finally, we compare the values of kinetic energy and free energy in Fig. 3, with each averaged over spherical surfaces, as a function of distance from the droplet center. For the stationary droplet, physically the kinetic energy should be zero. However, a low level of spurious currents usually exists near the fluid-fluid interface in simulations.^{5,11,62,63,67–73} Indeed, a small non-zero kinetic energy is found to exist in the stationary droplet simulation near the interface. Fig. 3(a) shows



(a) $t^* = 0$ (LHS) and $t^* = 39.1$ (RHS)



(b) ϕ in the center line of x direction

FIG. 1. The profiles of the order parameter at different times. The curve marked “Analytical” represents Eq. (31).

that the kinetic energy remains stable after about $t^* = 19.5$. Compared to Fig. 3(b), we conclude that the energy from spurious currents is much smaller than the free energy, by a factor of about 2×10^{-8} in this case, and thus the former can be safely neglected. Fig. 3(b) also shows that the free energy distribution is almost independent of time and close to the approximate analytical result during the evolution process of the stationary droplet.

In summary, the simulation results for a stationary droplet in 2D and 3D indicate that the PF-DUGKS approach yields physically accurate results, with a stable spherical drop being maintained

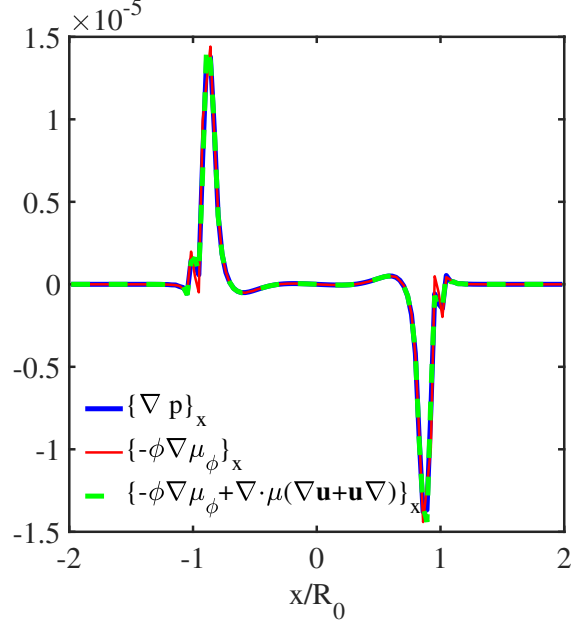


FIG. 2. Momentum balance along the center line in x direction at $t^* = 39.1$.

over time, a good mass conservation and momentum balance, and negligible spurious currents. This provides a basis for us to apply the approach to turbulent immiscible two-phase flows, to be discussed next.

IV. A FREELY-DEFORMING DROPLET IN DECAYING TURBULENCE

In this section, we apply the PF-DUGKS code to perform DNS of a freely-deforming droplet in decaying turbulence to (1) test our code in a turbulent background flow, (2) demonstrate that the PF-DUGKS model can also reproduce a single-phase flow in the limit of negligible surface tension, (3) demonstrate the application of a spherical harmonic spectral analysis, and (4) show the energy evolution in such a decaying background flow field.

A few main statistics of the flow are defined here, which are also used in the next section. The kinetic energy and dissipation rate per unit mass are computed from the energy spectrum $E(k, t)$, namely, $K(t) = (\mathbf{u}')^2/2 = \int E(k, t) dk$, $\varepsilon(t) = \int 2\nu k^2 E(k, t) dk$, where $\nu = \mu/\rho$ is the kinematic viscosity. The Taylor microscale Reynolds number is defined as $Re_\lambda = u'\lambda/\nu$, where the root-mean-square (r.m.s.) turbulent fluctuating velocity u' and the Taylor microscale λ are computed from $u' = \sqrt{\langle \mathbf{u}' \cdot \mathbf{u}' \rangle_V/3}$, $\lambda = \sqrt{15\nu/\varepsilon u'}$, here $\langle \cdot \rangle_V$ represents the volume average over the whole computational domain.

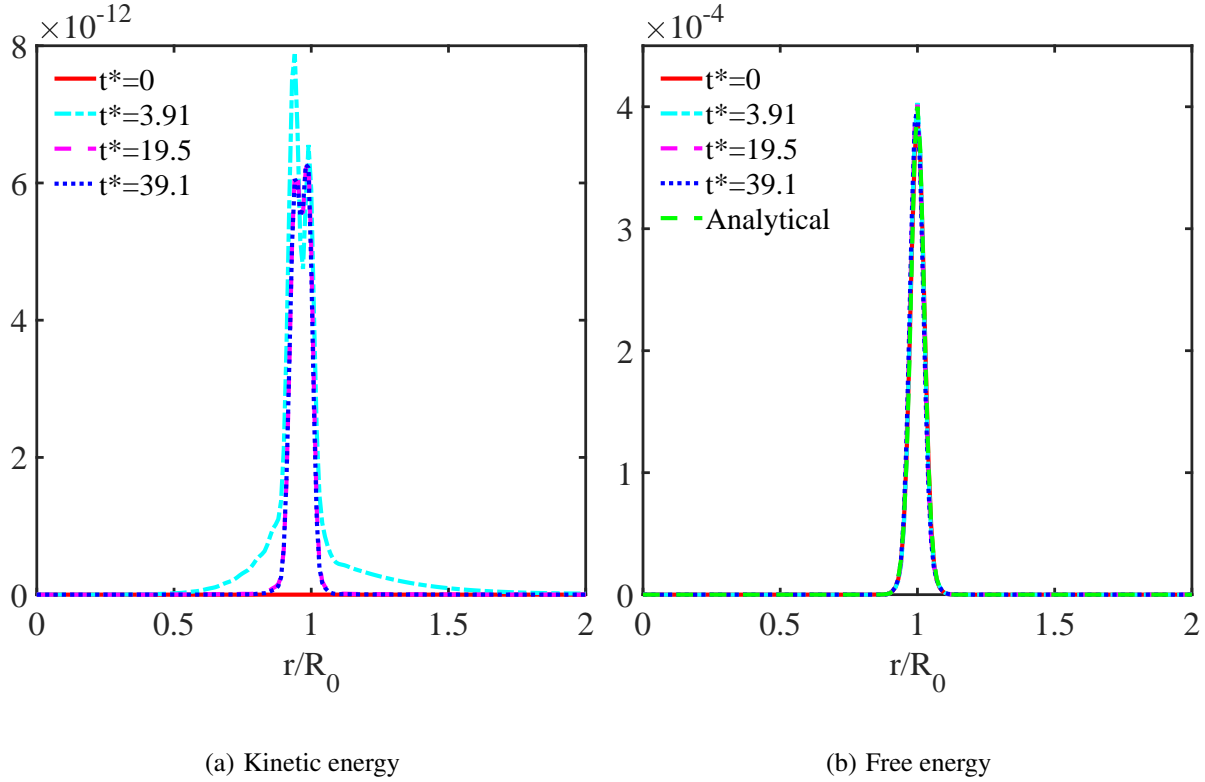


FIG. 3. Spherically averaged energies as a function of radial distance from the center of the initial droplet, at different times. The "Analytical" result in (b) is based on Eq. (31).

This droplet-deformation simulation case follows the work of Chen *et al.* (2019),⁴⁶ where they showed that the PF-DUGKS results are in good agreement with those based on solving the macroscopic governing equations such as the ARCHER code,⁴⁶ implying that the PF-DUGKS approach can generate reliable results for a two-phase decaying turbulence. The spatial grid resolution is 128^3 with periodic boundary conditions in all three directions. Wang *et al.* (2016)⁴² showed that DUGKS has a superior numerical stability particularly for high Reynolds number flows and can adequately resolve the turbulent flow when $k_{\max}\eta > 3$, where k_{\max} is the maximum resolved wave number and $\eta = (v^3/\epsilon)^{1/4}$ is the Kolmogorov length scale. In our simulation, the initial $k_{\max}\eta = 7.0$. The density ratio and the viscosity ratio of two-phase flow are both set to 1. The CFL number is 0.25. The initial maximum velocity magnitude is 0.034, satisfying the model assumption of an incompressible flow.

We consider two different settings. The first setting is referred to as the two-phase setting. Under the two-phase setting, we expect that the two-phase flow resembles the single-phase flow when the surface tension is set to a very small value, say $\sigma = 1.0 \times 10^{-20}$, yielding very large

Weber number and Capillary number (see below). Alternatively, in a second setting, referred to as the single-phase setting, ϕ is simply set to $\phi = \phi_B = 0$ in the whole computational domain, thus the chemical potential μ_ϕ and the interfacial force \mathbf{F} are both zero everywhere at all times. Then the CH equation (Eq. (6c)) and \mathbf{F} in the momentum equation (Eq.(6b)) can be neglected in theory. The governing equations then become identical to those in a single-phase flow. It follows that in the single-phase setting, the value of σ plays no dynamic role and we can set this to any value; we set $\sigma = 1.0 \times 10^{-3}$ in the single-phase setting.

In order to set up a physical initial velocity field across the droplet interface, we follow the initialization procedure in Chen *et al.* (2019),⁴⁶ where a turbulent flow containing a solid particle is first simulated as follows. First, single-phase FHIT is generated using a linear forcing scheme.^{74,75} Second, a solid particle is introduced and the flow containing the solid particle continues to evolve without the large-scale forcing, for several large-eddy turnover times. This step allows the flow near the solid particle surface to settle properly. The above flow simulations were performed using a finite-volume approach combined with the immersed boundary method.⁷⁶ This flow field was then used to initialize our PF-DUGKS code by replacing the solid particle with a droplet of the same volume. The initial values of \tilde{f} and \tilde{g} are constructed based on the given macroscopic flow field, namely, with the non-equilibrium distributions provided by the Chapman-Enskog analysis. The initialization is now done and the time is denoted as $t = 0$. Since the initialization is spherically symmetric and the magnitudes of the flow velocity inside and outside the droplet are quite different, a spectral analysis based on the spherical harmonics (See Appendix C 2) is more appropriate when analyzing the droplet deformation after its initial release. For the two-phase setting, the initial radius of the droplet is $R_0 = 31.74$ lattice units, ensuring a good resolution of the flow inside the droplet. Therefore, the initial Weber number for two-phase flow is $We = \rho u'^2 R_0 / \sigma = 2.48 \times 10^{17}$ and the initial Capillary number $Ca = \mu u' / \sigma = 1.64 \times 10^{16}$, which means that the surface tension plays no dynamic role in this case. The volume fraction is $V_{drop}/V_{box} = 0.064$. The initial interfacial thickness parameter $W = 3.0$, giving a small Ch number $Ch = W/R_0 = 0.095$. The dimensionless time is defined as $t^* = t\varepsilon(0)/K(0)$, where $K(0)$ and $\varepsilon(0)$ are the initial kinetic energy and initial dissipation rate, respectively. The initial velocity magnitude field is shown in Fig. 4.

Fig. 5 shows the evolution of fluid-fluid interface in the decaying turbulent flow under the two-phase settings, illustrating the complex distortion of the passive droplet interface as a function of time. At the early time $t^* = 0.98$, the droplet is only slightly deformed. At $t^* = 3.91$, the interface

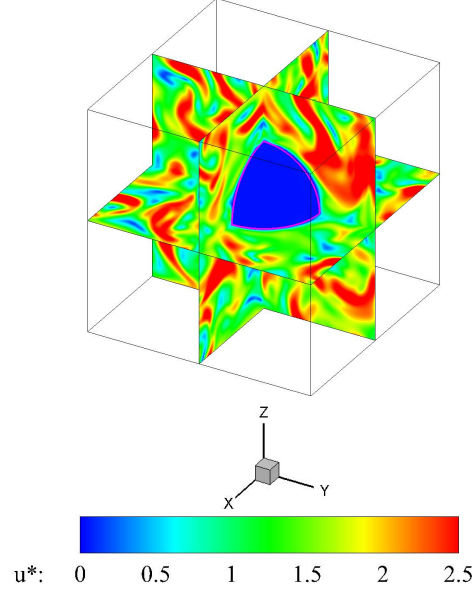


FIG. 4. Dimensionless velocity magnitude $u^* = |\mathbf{u}| / [u'(t^* = 0)]$ on the center planes at the initial state. The purple lines mark the intersection between droplet surface $\phi = 0.5$ and the central planes for the two-phase setting.

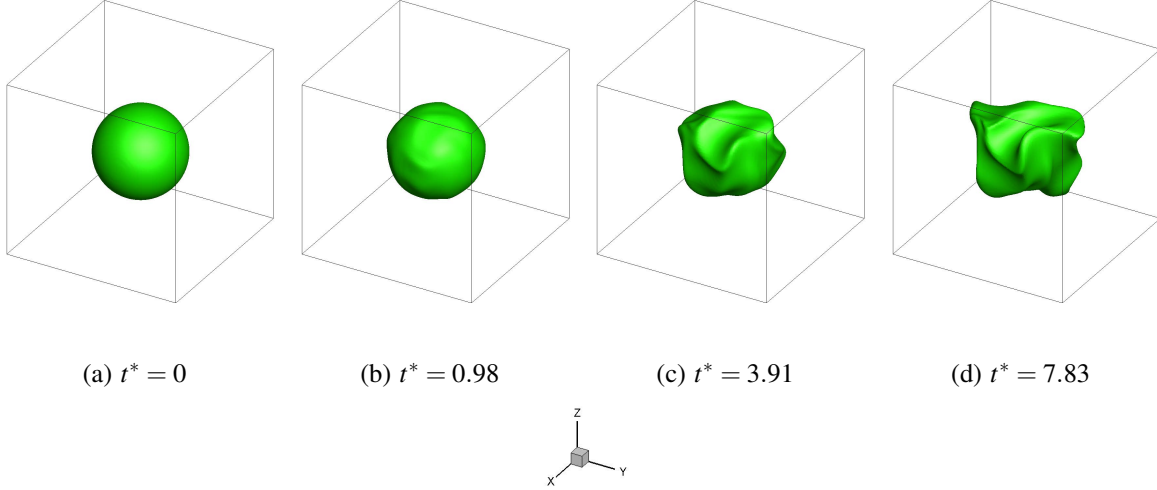


FIG. 5. 3D visualization of a droplet deformation in a decaying turbulent flow at different dimensionless times. The surface is given by $\phi = 0.5$.

becomes much more complicated, with distinct depressions and bulges.

The total kinetic energy decreases rapidly between $t^* = 0$ and $t^* = 0.98$ due to the specific initialization used, followed by a relatively slow decay of the total kinetic energy from $t^* = 0.98$ to $t^* = 3.91$. The total kinetic energy at $t^* = 0, 0.98, 3.91$ are 152.80, 83.34, 32.74, respectively.

Fig. 6 compares the energy spectra based on the spherical harmonics, showing an excellent agreement between the two-phase setting and single-phase setting of the PF-DUGKS code, for all distances from the initial droplet center and all times. Here l represents the wavenumber on a spherical surface of a given radius r , meaning that $E(l)$ represents the kinetic energy associated with velocity fluctuations at the length scale of r/l . To properly compare the energy level at a same length scale, we therefore set the horizontal axis in Fig. 6 to lR_0/r . Since both the single-phase and two-phase settings are designed to eliminate the surface tension effect, the identical results obtained here validate the PF-DUGKS code. Furthermore, Fig. 6 indicates that the kinetic energy outside the initial droplet region will decay due to two reasons: first, the viscous dissipation takes away kinetic energy as no external forcing is applied. Second, the kinetic energy in the outer region is transported to the region near and inside the droplet where the initial kinetic energy is low, causing a fast decay of energy outside and a quick increase of kinetic energy inside, during the initial evolution stage. Eventually, the spectrum shapes are similar inside and outside the droplet, for high wavenumbers of wavelengths much less than the radius r , as confirmed in Fig. 6(d). For lower wave numbers of wavelengths comparable to r , the spherical harmonic modes are different for different r , yielding different energy spectra for different r . Therefore, the spherical harmonic energy spectra provide a way to represent energy transport between different r as well as different scales at a given r .

Fig. 7 shows the kinetic energy and free surface energy averaged over a spherical surface as a function of the distance from the initial droplet center. Fig. 7(a) clearly demonstrates the fast decay of kinetic energy outside the droplet and transport of kinetic energy into the droplet, as noted already in Fig. 6. Fig. 7(b) shows the evolution of free energy from the two-phase setting. Initially, the profiles of free energy $F(\phi)$ are localized near the interface $r/R_0 = 1$. As time evolves, the interface expands to the regions inside and outside the initial spherical droplet. Therefore, the profiles of free energy also expand, being wider with smaller peak amplitudes, and then their shape becomes more and more irregular. The magnitude of the free energy is on the order of 10^{-21} , 16 orders of magnitude smaller than that of the kinetic energy, confirming that the free energy can be safely neglected here. Note that the relative difference in magnitude roughly mimics the initial Weber number (2.48×10^{17}) noted before, so the Weber number could be viewed as the ratio of kinetic energy to free energy.

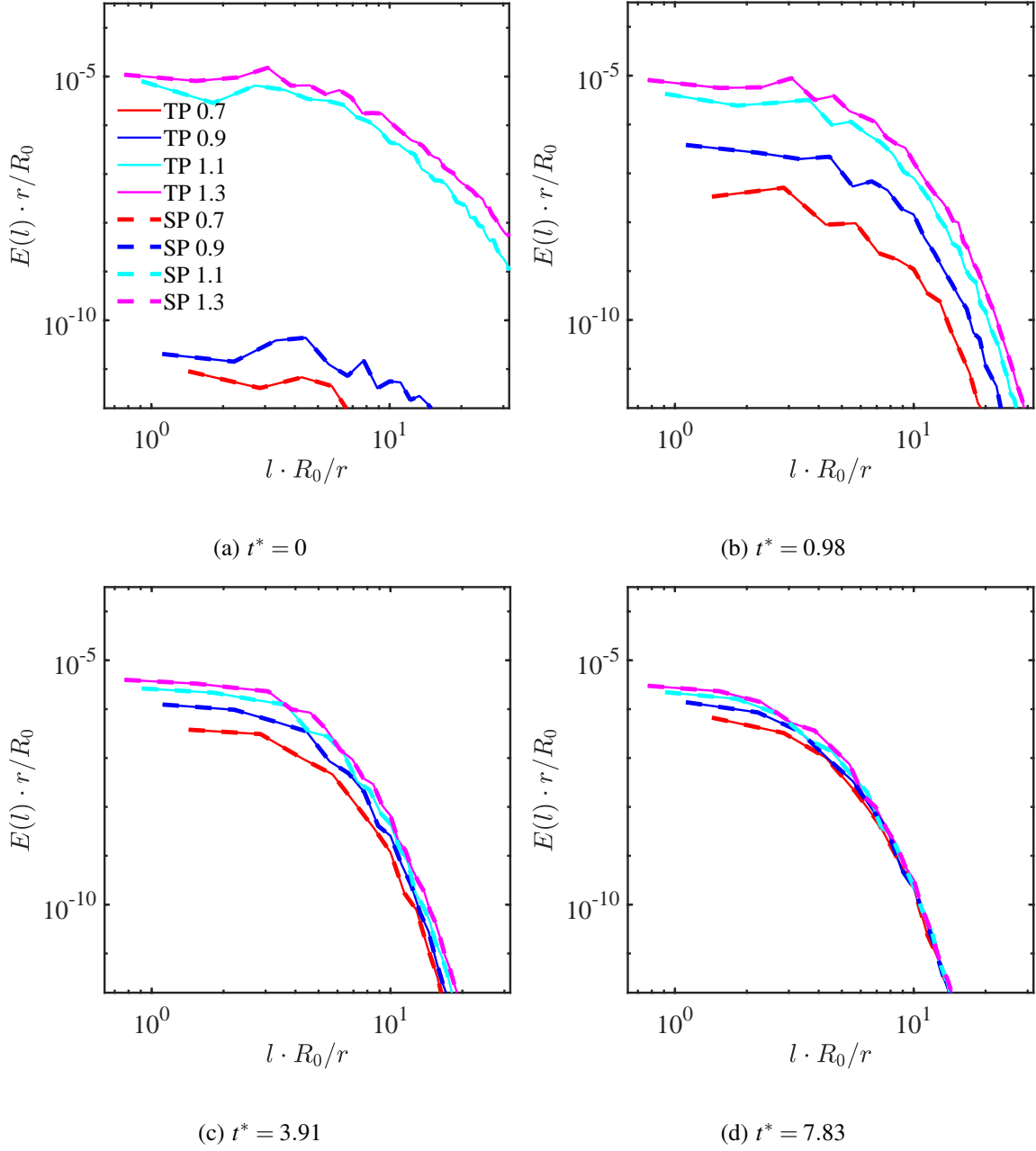


FIG. 6. Energy spectra on the spherical surfaces at different times for the two-phase (TP) flow ($We = 2.48 \times 10^{17}$) and the single-phase (SP) flow. The surface location is indicated by the normalized radii, $r/R_0 = 0.7, 0.9, 1.1, 1.3$. The initial radius of the droplet is $R_0 = 31.74$.

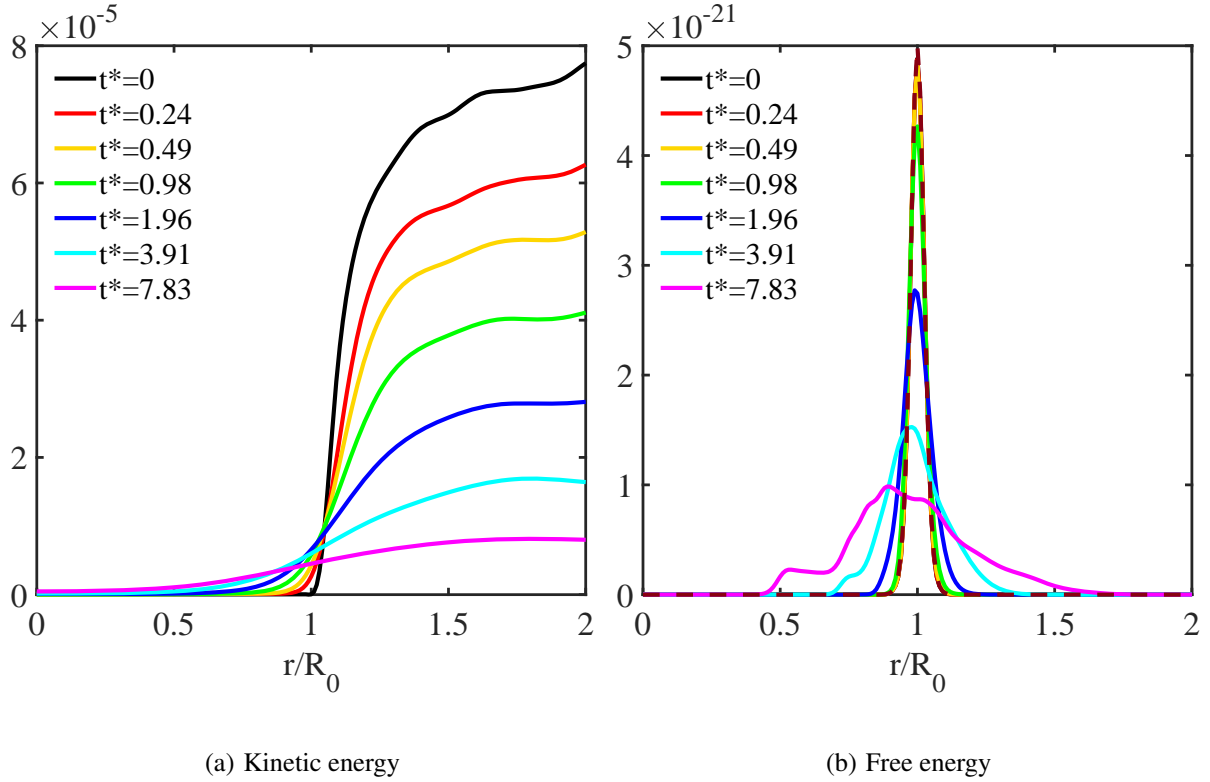


FIG. 7. Spherical-surface averaged energies as a function of radial distance, at different times for the two-phase setting. The dark red dashed line in (b) is the initial analytical result based on Eq. (31).

V. BREAKUP OF A SPHERICAL DROPLET IN DECAYING HOMOGENEOUS ISOTROPIC TURBULENCE

A. Problem setup and initialization

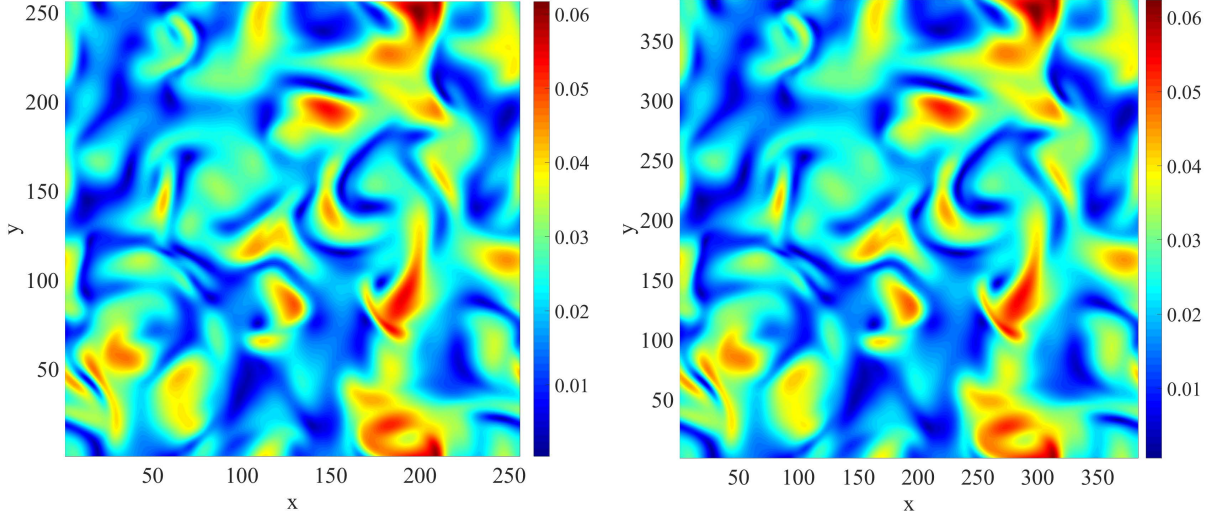
In this section, we apply the PF-DUGKS method to simulate the breakup process of a spherical droplet in DHIT. The computational domain is a cubic box containing 256^3 lattice nodes with periodic boundary conditions in all directions. The density ratio and the viscosity ratio are set to be unity. We first initialize a DHIT field using a single-phase setting. The initial order parameter ϕ and pressure field p are both set to zero. The initial velocity field \mathbf{u} in this single-phase setting is specified by a Gaussian field with a prescribed kinetic energy spectrum,^{42,77} $E(k) = Ak^4 e^{-0.14k^2}$ for $k_{\min} \leq k \leq k_{\max}$, where k is the wavenumber, $k_{\min} = 2$ and $k_{\max} = 10$ are selected in our simulation. The constant parameter A is set 5.0×10^{-6} . The initial velocity field of single-phase flow in the physical space is obtained by inverse Fourier transform. The maximum velocity magnitude of this single-phase initialization is 0.0988, which ensures a sufficiently small Mach number that is

consistent with our nearly incompressible DUGKS formulation.

We first compare the single-phase velocity magnitude field computed by the PF-DUGKS method, under the single-phase setting (*i.e.*, $\phi = 0$), with that computed by the pseudo-spectral (PS) method. We first run the PF-DUGKS code for a period of time till the pressure field is properly initialized to be consistent with the velocity field. At this point, $Re_\lambda = 76$, $k_{\max}\eta = 3.6$, and we extract the velocity field and share with the PS code. We use the $2/3$ - *rule* in the spectral method to remove the aliasing error,^{78,79} hence the computational domain is set to a cubic box with 384^3 nodes in the PS code. After about 0.1 large-eddy turnover times, we obtain the velocity fields from these two codes, and compare with each other. Fig. 8 shows the velocity magnitude contours on a same center plane. Fig. 9 plots the velocity magnitude profiles on the same center lines in three directions. Both figures show almost the same results from the two approaches. Furthermore, we also calculate the correlation coefficient of three components of the velocity over the whole domain, *i.e.*, u_x , u_y , u_z , between these two approaches. The results for $\text{Corr}(u_x(\text{PF-DUGKS}), u_x(\text{PS}))$, $\text{Corr}(u_y(\text{PF-DUGKS}), u_y(\text{PS}))$, $\text{Corr}(u_z(\text{PF-DUGKS}), u_z(\text{PS}))$ are 0.9999, 0.9999, 0.9998, respectively. Here the correlation coefficient $\text{Corr}(s_1, s_2)$ of arbitrary scalar fields s_1 and s_2 is $\text{Corr}(s_1, s_2) = \frac{\langle (s_1 - \langle s_1 \rangle_V)(s_2 - \langle s_2 \rangle_V) \rangle_V}{\sqrt{\langle (s_1 - \langle s_1 \rangle_V)^2 \rangle_V \langle (s_2 - \langle s_2 \rangle_V)^2 \rangle_V}}$. These comparison results again demonstrate that the PF-DUGKS code can accurately simulate the evolution of a single-phase turbulence with adequate resolution.⁴²

Now the above velocity field calculated by PF-DUGKS method (Fig. 8(a)) is used as the initial velocity field for the two-phase flow setting. We add a spherical droplet in this flow field, *i.e.*, reset the order parameter ϕ with Eq. (31). This moment is now viewed as $t = 0$ for the discussions below.

The maximum velocity and vorticity magnitudes at the two-phase flow initialization are $|\mathbf{u}(t^* = 0)|_{\max} = 0.0822$ and $|\boldsymbol{\omega}(t^* = 0)|_{\max} = 0.0238$, respectively. The r.m.s. velocity and vorticity of two-phase initialization are $u'(t^* = 0) = 0.0165$ and $\omega'(t^* = 0) = 0.0023$, respectively, where $\omega' = \sqrt{\langle \boldsymbol{\omega}' \cdot \boldsymbol{\omega}' \rangle_V / 3}$. The surface tension is set to $\sigma = 8.0 \times 10^{-4}$, the density and kinematic viscosity are set to 1.0 and 4.5×10^{-3} , respectively, for both phases. The initial droplet radius R_0 is 64 (the initial droplet diameter is $D_0 = 128$), the interfacial thickness parameter is $W = 3$. These settings imply the following initial dimensionless parameters: the Taylor microscale Reynolds number Re_λ is 58, $Ch = 0.0469$, the dispersed phase volume fraction ϕ is 6.54%, the Weber number We is 21.66, and $k_{\max}\eta$ is 3.28 (which is sufficient to resolve the smallest turbulence scales).⁴² Since no external forcing is applied, both of the Weber number and Reynolds number



(a) PF-DUGKS method

(b) PS method

FIG. 8. Contours of velocity magnitude on the center plane in the z direction at $t^* = 0$.

decrease with time.

The energy spectra of single-phase initialization and two-phase initialization are showed in Fig. 10. The kinetic energy mainly contains large scales at the single-phase initialization. Then the energy is transferred to the small scales over time when the two-phase flow simulation begins.

At this time, the velocity derivative skewness S_u is between -0.6 and -0.5 , which is reasonable for this flow field.^{42,61,80,81} Here $S_u = \frac{\langle [(\partial u_x/\partial x)^3 + (\partial u_y/\partial y)^3 + (\partial u_z/\partial z)^3]/3 \rangle}{\langle [(\partial u_x/\partial x)^2 + (\partial u_y/\partial y)^2 + (\partial u_z/\partial z)^2]/3 \rangle^{3/2}}$.

Additionally, we also simulate another single-phase (*i.e.*, $\phi = 0$) DHIT using the same code and the same velocity field and pressure field at $t^* = 0$, in order to compare the results with those from the two-phase flow setting when necessary. It is noted that, unlike Section IV, here the two-phase setting is expected to yield different results from the single-phase setting as the surface tension now can play a role. In fact, due to the turbulence decay, the Weber number will decrease monotonically, from 21.66 to less than 0.01 (see later discussions in Section V B), implying that the surface tension eventually plays a more important role in determining the interfacial dynamics, than the turbulent kinetic energy.

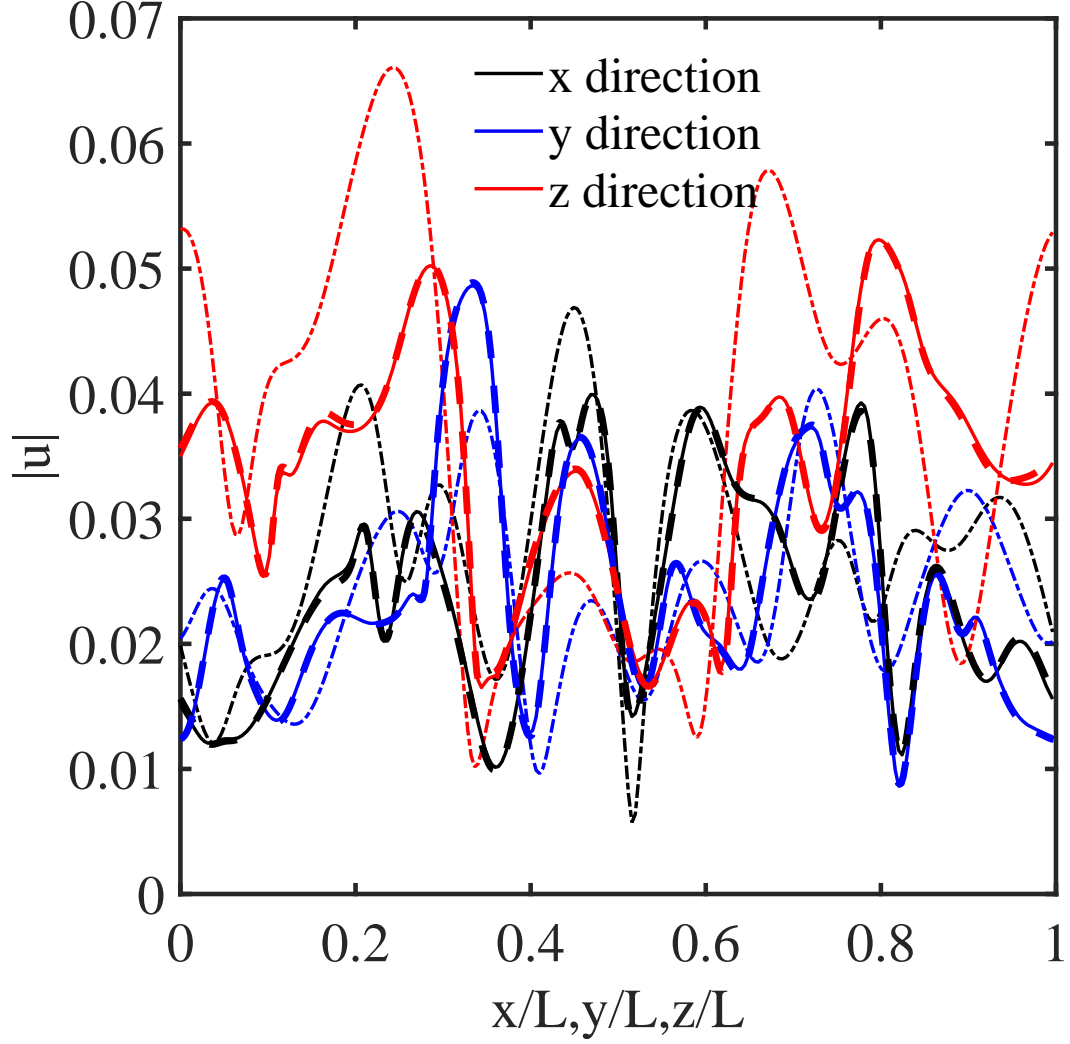


FIG. 9. Velocity magnitude profiles of the single-phase flows along the centerlines in the x, y, z directions. L is the computational box size. $L = 256$ for the PF-DUGKS method, while $L = 384$ for the PS method. The thin solid lines represent the velocity magnitude calculated by the PF-DUGKS method at $t^* = 0$, and the thick dashed lines represent the velocity magnitude calculated by the PS method at $t^* = 0$. The thin dash-dot lines represent the velocity profiles that are shared with the PS method, at $t^* = -0.1$.

B. Three stages of fluid-fluid interface evolution

Fig. 11 shows the evolution of the droplet shape at different dimensionless times, where $t^* = t\varepsilon(0)/K(0)$. The initial shape is a sphere located at the center of the box. This droplet may deform and break up due to the turbulent background flow. As noted by Qian *et al.* (2006)⁸ and Albernaz *et al.* (2017),³ no simple criterion related to breakup could be identified. Hinze (1955)³⁴ argued that the competition of capillary pressure and pressure fluctuations due to turbulent eddies

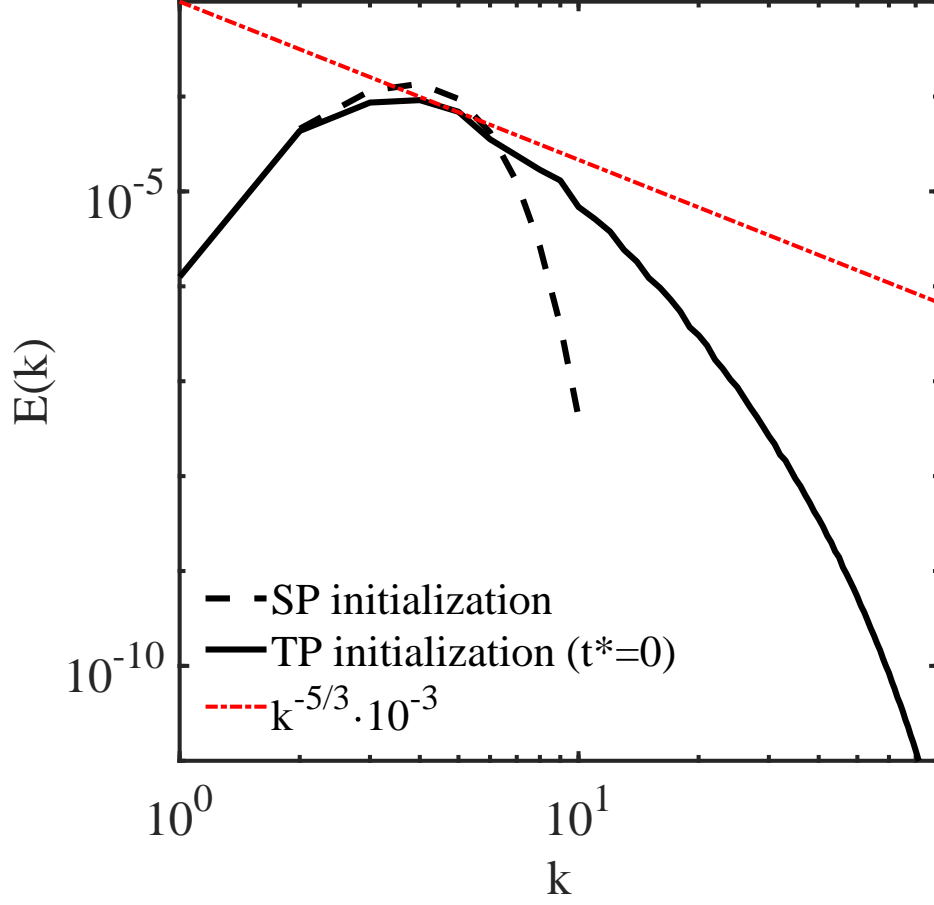


FIG. 10. The kinetic energy spectrum used to initialize the single-phase (SP) and two-phase (TP) flow simulation, respectively.

determines the characteristic diameter D_c of the droplets in turbulence. Assuming the inertial-subrange scaling, he obtained that $D_{\text{Hinze}} = C(\sigma/\rho)^{3/5} \varepsilon^{-2/5}$ in HIT background flow field. This criterion can also be derived based on the dimensional analysis, if one assumes that only the physical quantities $\rho, \sigma, \varepsilon$ determine D_{Hinze} .³⁴ Here $C = 0.725$ based on Clay (1940)'s experimental observations.^{34,82} While the flow Reynolds number in our simulation is too low to have the inertial subrange, we will nevertheless apply the Hinze criterion as an estimate. According to the Hinze criterion, at $t^* = 0$, the maximum droplet diameter that does not undergo breakup can be estimated to be $D_{\text{Hinze}} \sim 7.20$ in our simulation (see Fig. 12). It is noted that D_{max} in Fig. 12 is computed by first obtaining the volume of the largest inter-connected $\phi \geq 0.5$ region, then $D_{\text{max}} \equiv \sqrt[3]{6V_{\text{max}}/\pi}$. Clearly, the droplet with $D_0 = 128.0$ placed in the flow can certainly break up. Indeed, as seen in Fig. 11, the droplet surface becomes wrinkled and stretched, and breaks down into many small irregular parts. According to Fig. 11, a spherical droplet breakup in DHIT can be divided into three

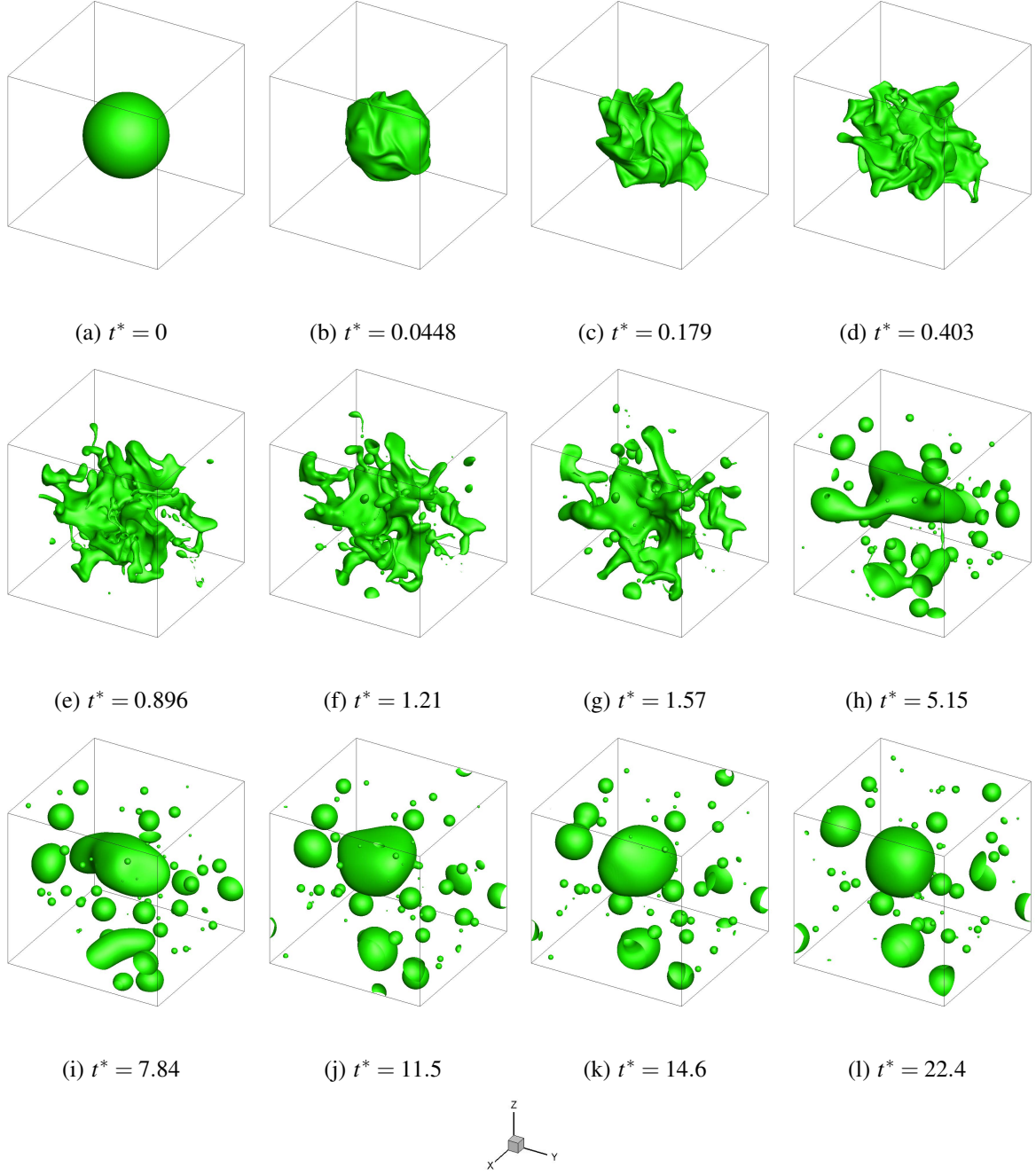


FIG. 11. 3D visualization of a droplet breakup in a DHIT flow at different normalized times. The surface is given by $\phi = 0.5$.

stages: (1) the deformation stage, where the large spherical droplet evolves into an irregular geometric pattern with complex interface structures, (2) the breakup stage, during which many small droplets are separated from the large one, (3) the restoration stage, during which all the droplets become spherical or merge with the nearby droplets, finally reaching a quasi-stationary state. The

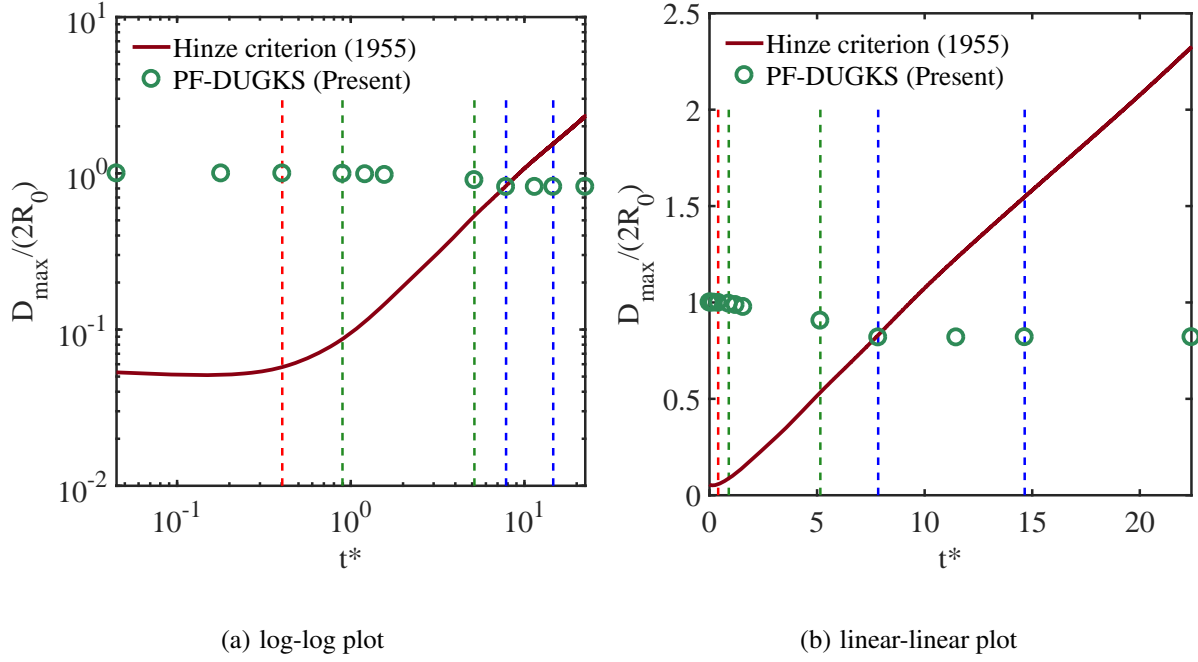


FIG. 12. The normalized maximum droplet diameters D_{\max} at different times in Fig. 11, comparing with the Hinze criterion. The different times correspond to the times in Fig. 11. $R_0 = 64.0$ is the radius of the initial droplet. The red, dark green, blue vertical dash lines mark typical times for deformation ($t^* = 0.403$), breakup ($t^* = 0.896$ and 5.15), restoration ($t^* = 7.84$ and 14.6), respectively.

deformation stage takes the shortest time, while the restoration stage takes the longest time, as the kinetic energy decreases with time in a power-law form in DHIT. Hence the logarithmic coordinates are usually used for time in the figures for this physical problem.

The first row in Fig. 11 (Fig. 11(a)-11(d)) is at the deformation stage. The turbulent kinetic energy disrupts the free energy equilibrium, augmenting the free energy of the system through increased interface area. The initial smooth spherical droplet develops irregular wrinkles on the whole interface. Then the wrinkles gradually elongate and intertwine in all directions, sometimes creating holes and changing the topological structure. At the end of this stage, the geometric structure is very complicated and the interface area is increased by a factor about 4.2 comparing to the initial state (see Fig. 13). It is noted that $We = 10.66$ and $Re_\lambda = 30$ at $t^* = 0.403$ (see Fig. 11(d) and Fig. 14). Therefore, during the first stage the velocity and pressure fluctuations in turbulence usually serve as the driving mechanism for droplet deformation. The surface tension force and viscous force act as a resistance to deformation.

The second row in Fig. 11 (Fig. 11(e)-11(h)) shows the interface evolution at the breakup

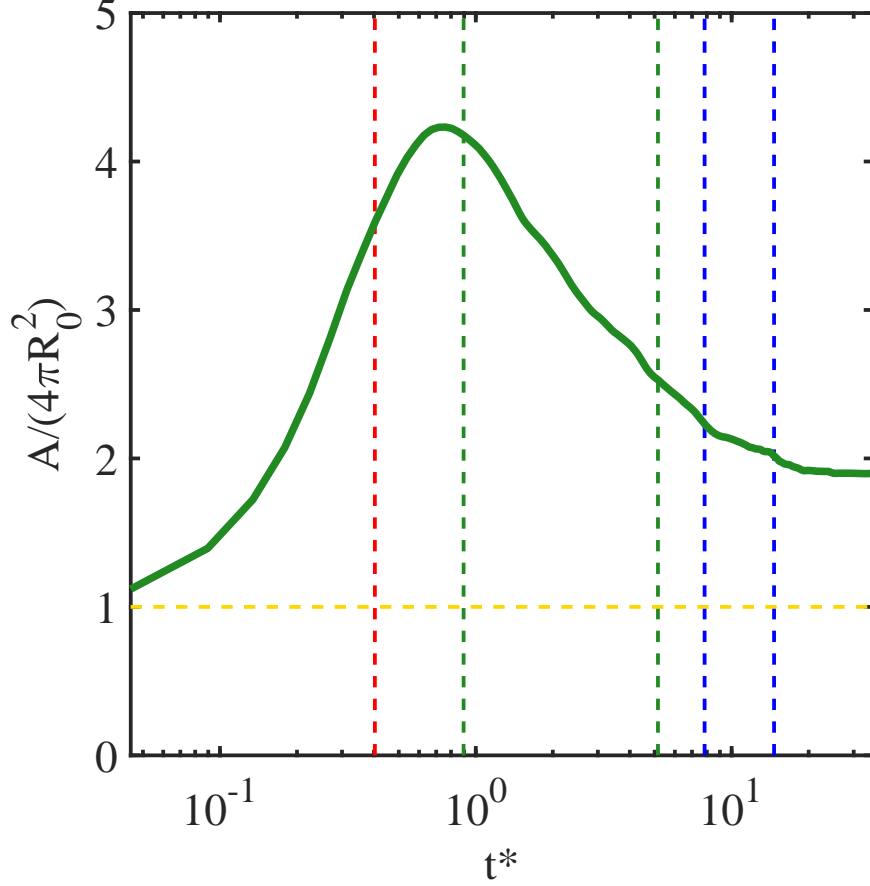


FIG. 13. Evolution of the normalized total interface area. The total area A is the area of isosurface $\phi = 0.5$. Initially, $A(t^* = 0) = 4\pi R_0^2$. The dashed yellow line is the constant 1. The vertical lines mark $t^* = 0.403, 0.896, 5.15, 7.84, 14.6$, respectively.

stage. The final state of the deformation stage provides adequate conditions for this breakup stage. The local volume distribution of the droplet phase is very nonuniform. Then regions where the cross-sectional areas of the droplet phase are small, may separate to generate daughter droplets. The factors that affect fragmentation include the following four aspects: (1) the fluid inertia developed during the deformation stage, which will continue to elongate the interface resulting in fragmentation, (2) the local pressure inside the droplet near the narrow neck is larger due to large local interface curvature, causing a local interfacial instability to develop which eventually leads to neck breakup (Similar idea was proposed by Qian *et al.* (2006),⁸ where they suggested that the capillarity effect causes breakup in a highly elongated region), (3) the velocity and pressure fluctuations also influence the breakup process, during which the droplet-breakup may be locally promoted or suppressed depending on the nature of the fluctuations, (4) viscous force acts to retard

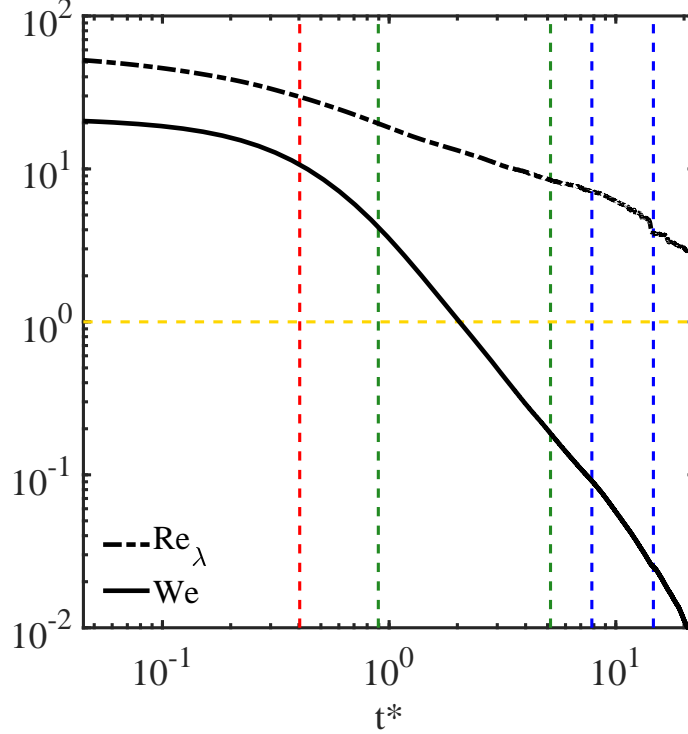


FIG. 14. Evolution of the dimensionless parameters Re_λ and We . Here $We = \rho u^2 R_0 / \sigma$. The dashed yellow line marks the constant one. The red, dark green, blue vertical dashed lines mark typical times for deformation ($t^* = 0.403$), breakup ($t^* = 0.896$ and 5.15), restoration ($t^* = 7.84$ and 14.6), respectively.

the breakup process. At the same time, the daughter droplets become convex and spherical in the breakup stage due to the influence of surface tension acting on decreasing the interface area, as shown in Fig. 13. The competition of inertial force/viscous force and inertial force/surface tension force are presented by Re_λ and We in Fig. 14, respectively. The dominant factor is the inertial force at the beginning of this stage, and is switched to the surface tension force at the end of this stage. As a result, this stage is the most complicated among the three stages. We can observe many small structures in Fig. 11(e), resolved by the adequate grid resolution applied.

The third row in Fig. 11 (Fig. 11(i)-11(l)) shows the interface evolution at the restoration stage. Take $t^* = 7.84$ (see Fig. 11(i) and Fig. 12), $D_{\text{Hinze}} \sim 106.33$, while the largest droplet diameter in the simulation is $D_{\text{max}} \sim \sqrt[3]{6V_{\text{max}}/\pi} = 104.84$. This implies that the breakup may stop around this time. The velocity and pressure fluctuations are now small because of the decay of kinetic energy, they then have less influence on the motion of droplets. The droplets cannot break up any more, while continue to become convex and spherical due to decreasing Weber numbers (Fig. 14). Fig. 14 also shows that the surface tension force is the driving force at this stage. The viscous force

TABLE II. The influence of various factors on different stages

	deformation stage	breakup stage	restoration stage
turbulence (inertial force)	$+(-)$	$+(-)$	$-(+)$
viscous force	$-$	$-$	$-$
surface tension force	$-(+)$	$-(+)$	$+$

'+' represents 'promote', '-' represents 'prevent'. ' $+(-)$ ' represents 'usually promote but sometimes prevent'.

still acts as the resistance. When two droplets are close to each other, the smaller one could be merged into the larger one. Fig. 11(j) shows the coalescence of a large droplet and a small droplet, and in Fig. 11(k) the coalescence of two medium-sized droplets are observed, during that time the total interface area will change a little bit as the droplet shape changes. The merging phenomenon increases the local velocity magnitude in the region between the merging droplets (see Fig. 17(d)). The droplets will become quasi-stationary at the end of this stage, continuing to evolve and merge slowly. The total interface area decreases due to restoration, while increases in the early part of coalescence process. The overall trend is a decreasing interface area and minimization of the free energy (see Fig. 13).

Fig. 12 demonstrates that our results on the maximum droplet diameter seem to be in quantitative agreement with the Hinze criterion. The demarcation time between breakup stage and restoration stage can be defined by $t^*(D_{\max} = D_{\text{Hinze}})$, which is roughly 7.8 according to Fig. 12. Furthermore, Fig. 12 shows that the maximum droplet diameter does not change much during the whole evolution in DHIT, only about 0.8 times of the initial diameter, which means the maximum droplet volume at the end of the simulation is roughly half of the initial droplet volume.

The above three stages represent the competition among three factors: the turbulent fluctuations, the viscous force, and the surface tension force. The likely contributions of these factors to the three stages are summarized in Table II.

C. Evolution of the number of droplets and droplet diameter distribution

The variation of the total number of droplets as a function of time is shown in Fig. 15. Here we developed an algorithm to identify individual droplets (see Appendix B). A droplet is defined as a set of inter-connected lattice nodes with $\phi \geq 0.5$, from which the volume and the equivalent

diameter of the droplet can be determined. Droplets of volume one are not considered in the counting as they could not be resolved by the phase field model. At the deformation stage, the number N_d is on the order of 1, since the initial droplet is spherical and requires time to deform and break up. During the deformation stage, small droplets may detach from the large droplet. Then the value of N_d may be larger than one at the end of this stage. $N_d = 4$ at $t^* = 0.403$, which means there are three small droplets being generated by this time. At the breakup stage, many small daughter droplets are formed, and N_d quickly reaches the order of 10. N_d continues to increase to about 60 at the end of the breakup stage. During the restoration stage, N_d tends to decrease due to the coalescence events. Roughly speaking, $dN_d/dt^* \geq 0$ at the deformation and breakup stages, and $dN_d/dt^* \leq 0$ at the restoration stage. Perlekar *et al.* (2012)³³ also show N_d varies with time in their droplet-breakup simulation at the FHIT background flow. They point out that the volume fraction ϕ and Reynolds number Re_λ will affect N_d . They found that N_d was roughly around 10, between 20 and 50, between 30 and 70, for $\phi = 0.5\%, 5\%, 10\%$, respectively, with $Re_\lambda = 15$ in their simulations. Our result $N_d \sim 60$ with $\phi = 6.54\%$ and initial $Re_\lambda = 58$ is reasonable compared to their results, since our flow Reynolds number is larger.

In order to observe the size distribution of droplets in the evolution process, we plot the probability distribution function of droplet radius in Fig. 16. The diameter is calculated by $D \equiv \sqrt[3]{6V/\pi}$. It is observed that, during the breakup stage (Figs. 16(a)-16(b)) and the restoration stage (Figs. 16(c)-16(d)), most droplets have a diameter smaller than 10% of the initial droplet diameter, namely, 84.4%, 62.7%, 61.0%, 63.5% of droplets in number are with a diameter less than $0.1D_0$, at $t^* = 1.21, 5.15, 11.5, 22.4$, respectively. At $t^* = 1.21$, the large droplet remains in one piece, and only the small droplets are formed from the highly distorted parts of the interface, hence the ratio is quite large, over 80%. Later the medium-size droplets are separated from the main part of the large droplet, due to the strong deformation of the large droplet. As a result, the ratio becomes smaller and reach a stable value around 60%. The diameter of the largest droplet is about 80% of the initial D_0 in the end, so it is always close to 1 in the log-log plot (Fig. 16) during the whole evolution. The vertical red line marks the location of the Kolmogorov scale. It is observed in Fig. 16 that more and more droplets become smaller than the Kolmogorov scale when time proceeds, namely, 2.2%, 13.6%, 33.9%, 57.7% of the droplets are smaller than η in diameter, respectively.

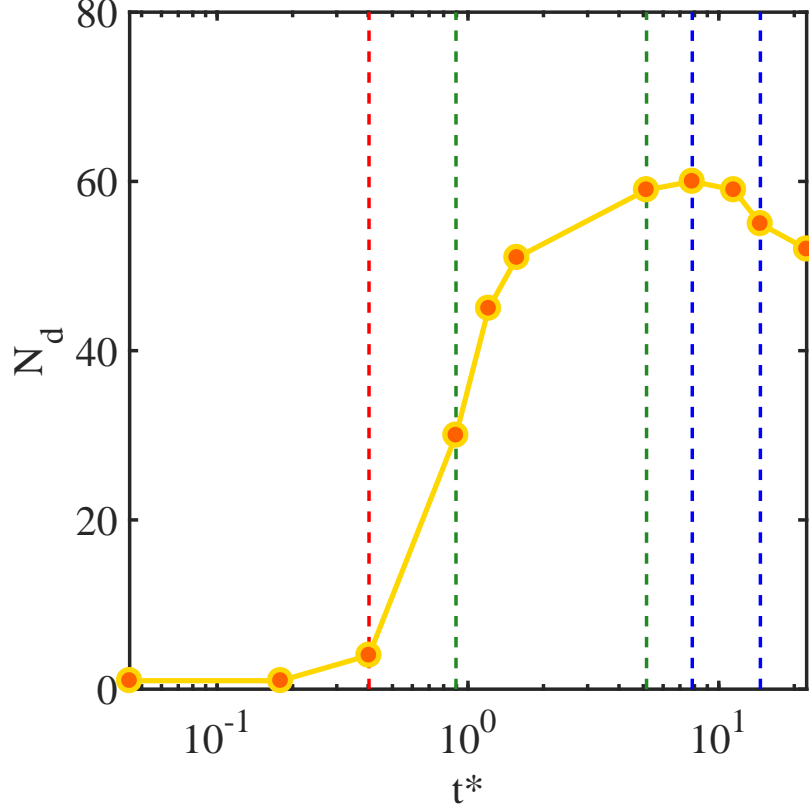


FIG. 15. The number of droplets (N_d) at different times in Fig. 11. The red, dark green, blue vertical dashed lines mark typical times for deformation ($t^* = 0.403$), breakup ($t^* = 0.896$ and 5.15), restoration ($t^* = 7.84$ and 14.6), respectively.

D. Velocity and vorticity magnitudes on the fluid-fluid interface

Fig. 17 and Fig. 18 show the dimensionless velocity and vorticity magnitudes on the droplet surface, respectively. Table III provides the average velocity and vorticity magnitudes on the isosurface $\phi = 0.5$, compared with the average values in the whole computational domain. The four times shown in Table III are the same as that in Fig. 17-18.

At the two-phase initialization time ($t^* = 0$, Fig. 17(a) and Fig. 18(a)), the velocity magnitude field and vorticity magnitude field are irregularly distributed on the spherical surface, because of the initial homogeneous isotropic flow field. The interface averages of velocity magnitude and vorticity magnitude are slightly larger than their respective volume averaged values. It is a coincidence, because the droplets have just been put in and have not had any effect on the flow field. Later in the deformation stage ($t^* = 0.403$), the average velocity magnitude on the interface has decreased significantly, only 56% of the initial velocity magnitude on the fluid-fluid interface.

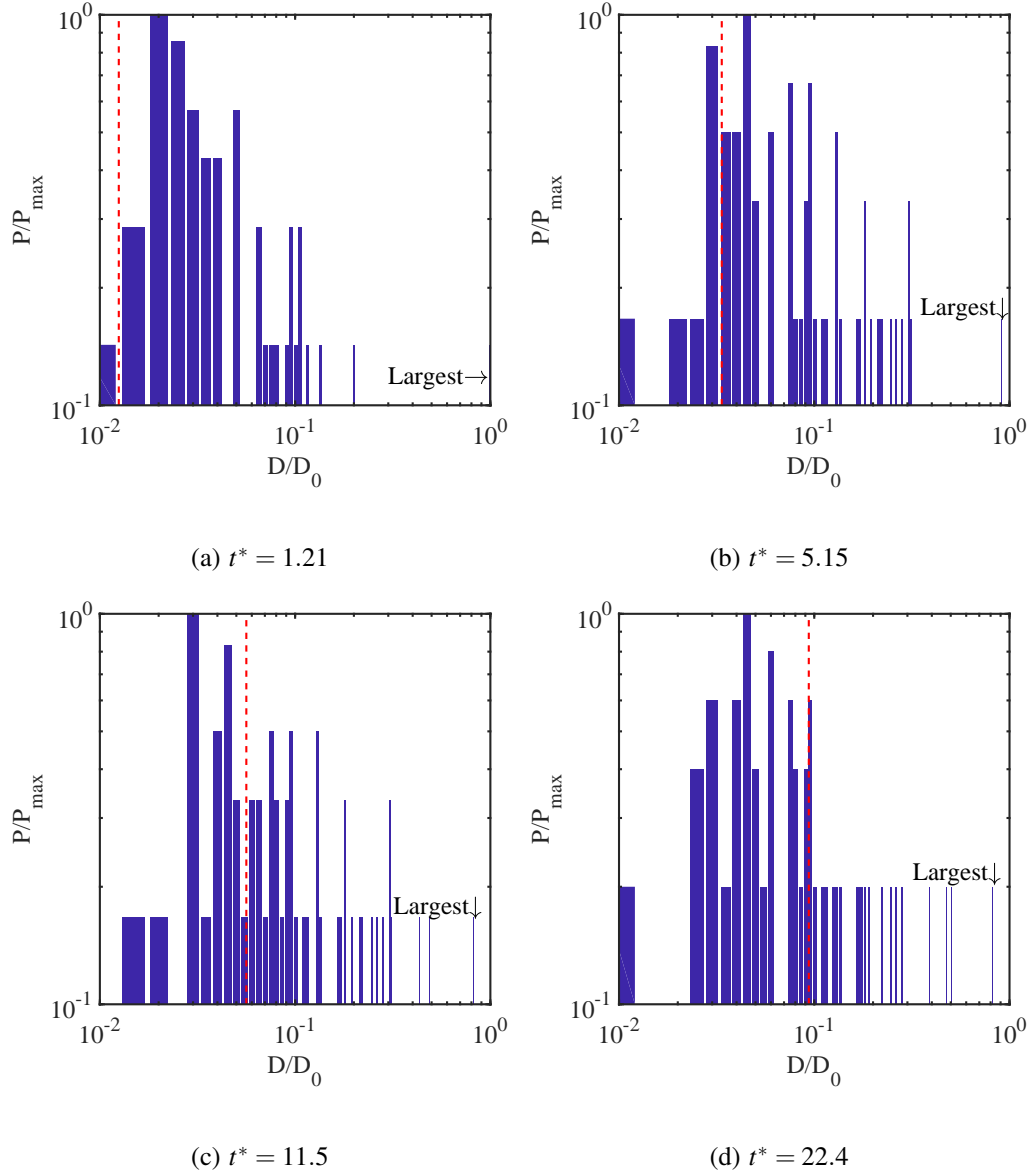


FIG. 16. Probability distribution function (PDF) of droplet diameter at different times. The red dashed line represents η/D_0 . The arrow points to the largest droplet.

The average velocity magnitude on the interface is roughly 20% less than that on the whole volume now, due to conversion of kinetic energy to the surface tension energy. From this point on, the average velocity magnitude on the interface continues to decrease relatively to the bulk region, showing that the surface tension force tends to damp the interface velocity magnitude, partially a reflection of the no-slip condition as the droplet interface have smaller velocity fluctuations.

The volume averaged vorticity magnitude decreases slowly, much slower than the reduction of velocity magnitude. It is interesting that the interface averaged vorticity magnitude is increased

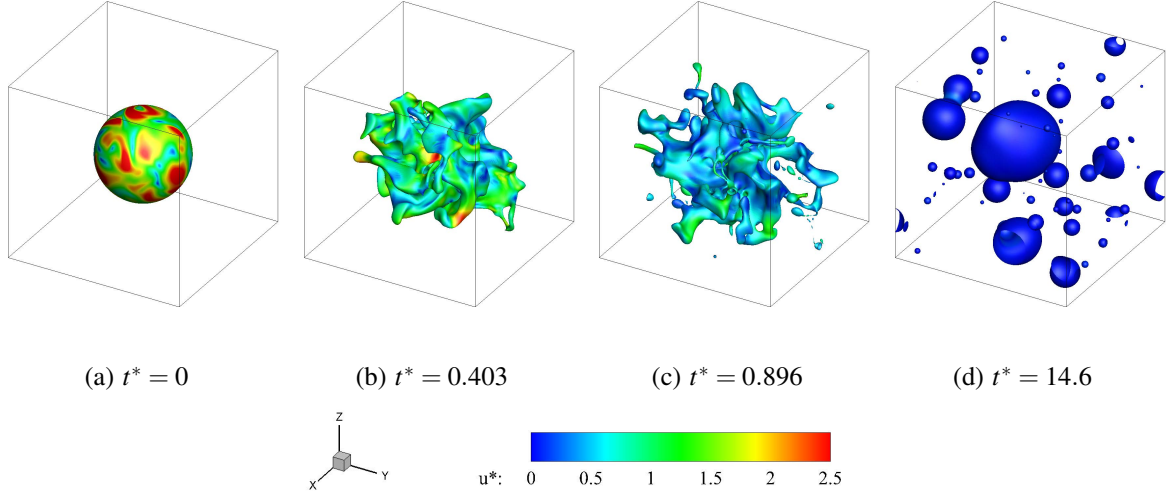


FIG. 17. Velocity magnitude $u^* = |\mathbf{u}| / [u'(t^* = 0)]$ on the fluid-fluid interface $\phi = 0.5$ at different times.

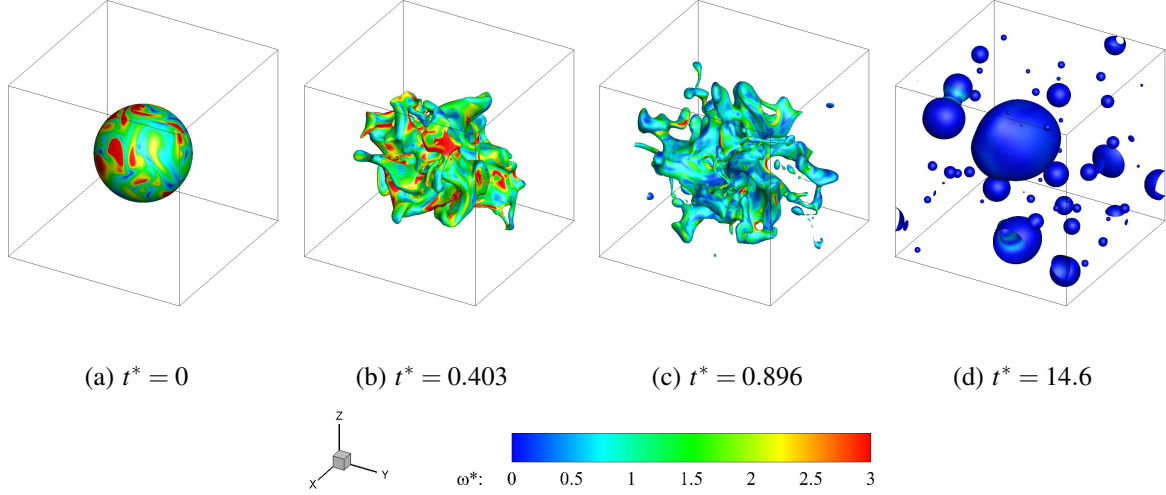


FIG. 18. Vorticity magnitude $\omega^* = |\boldsymbol{\omega}| / [\omega'(t^* = 0)]$ on the fluid-fluid interface $\phi = 0.5$ at different times.

slightly at $t^* = 0.403$, compared to the initial vorticity magnitude. The reasons are as follows. First, the averaged vorticity magnitude in the whole volume does not change much. Second, the wrinkling of the interface could generate localized small-scale flows and thus vorticity, also viscous boundary layers can develop near the interface. The interface averaged vorticity magnitude is always larger than the volume average vorticity magnitude, as showed in Table III. One of the reasons is that, the fluid-fluid interface can be viewed as a deformable viscous boundary layer, and vorticity can be produced there.

Fig. 17(c) and Fig. 18(c) are at $t^* = 0.896$, the early period of the breakup stage. The averaged velocity magnitude still decreases quickly. The averaged vorticity magnitude also decreases

TABLE III. The average velocity and vorticity magnitudes on the interface at different times.

	$t^* = 0$		$t^* = 0.403$		$t^* = 0.896$		$t^* = 14.6$	
	u^*	ω^*	u^*	ω^*	u^*	ω^*	u^*	ω^*
$\langle \cdot \rangle_S$	1.6053	1.6207	0.9024	1.7932	0.5009	0.9797	0.0077	0.0641
$\langle \cdot \rangle_V$	1.5767	1.5023	1.1189	1.4208	0.6944	0.8431	0.0533	0.0222
$\frac{\langle \cdot \rangle_S - \langle \cdot \rangle_V}{\langle \cdot \rangle_V}$	0.0182	0.0788	-0.1935	0.2621	-0.2786	0.1621	-0.8563	1.8851
$\frac{\langle \cdot \rangle_S - \langle \cdot \rangle_{S,t^*=0}}{\langle \cdot \rangle_{S,t^*=0}}$	0	0	-0.4379	0.1064	-0.6880	-0.3955	-0.9952	-0.9605
$\frac{\langle \cdot \rangle_V - \langle \cdot \rangle_{V,t^*=0}}{\langle \cdot \rangle_{V,t^*=0}}$	0	0	-0.2904	-0.0543	-0.5596	-0.4388	-0.9662	-0.9852

$\langle \cdot \rangle_S$ denotes the average value on the fluid-fluid interface at $\phi = 0.5$. $\langle \cdot \rangle_V$ refers to the average values in the whole computational domain.

quickly now, compared to the previous stage. The interface averaged velocity magnitude is much smaller than the volume averaged velocity magnitude, compared to that at $t^* = 0.403$. Since the surface tension force continues to restrict the interface velocity, then the relative velocity magnitude on the interface decreases monotonically in time.

Fig. 17(d) and Fig. 18(d) display the results during the restoration stage at $t^* = 14.6$. The velocity and vorticity magnitudes are both very small now, and the averaged values are all less than 4% of the corresponding initial results, as showed in Table III. The interface averaged velocity magnitude is significant smaller, less than 0.5% of the initial value. However, the velocity magnitude is slightly larger between two colliding droplets when they merge with each other, as showed in Fig. 17(d); when they approach each other, the interface is deformed due to local hydrodynamic interaction and the nearby velocity magnitude could increase. The vorticity magnitude near the merging interface also increases with the increasing of velocity magnitude. At that time, the vorticity magnitude in the whole domain is very small (less than 1.5% of the initial result), while the interface boundary layers result in a relatively larger vorticity magnitude on the interface (about three times) than that in the whole volume (Table III).

E. Kinetic energy decay

Fig. 19 shows the evolution of the normalized total kinetic energy $K^* = K(t)/K(0)$ and the normalized dissipation rate $\varepsilon^* = \varepsilon(t)/\varepsilon(0)$. In Fig. 19(a), the single-phase flow results from two

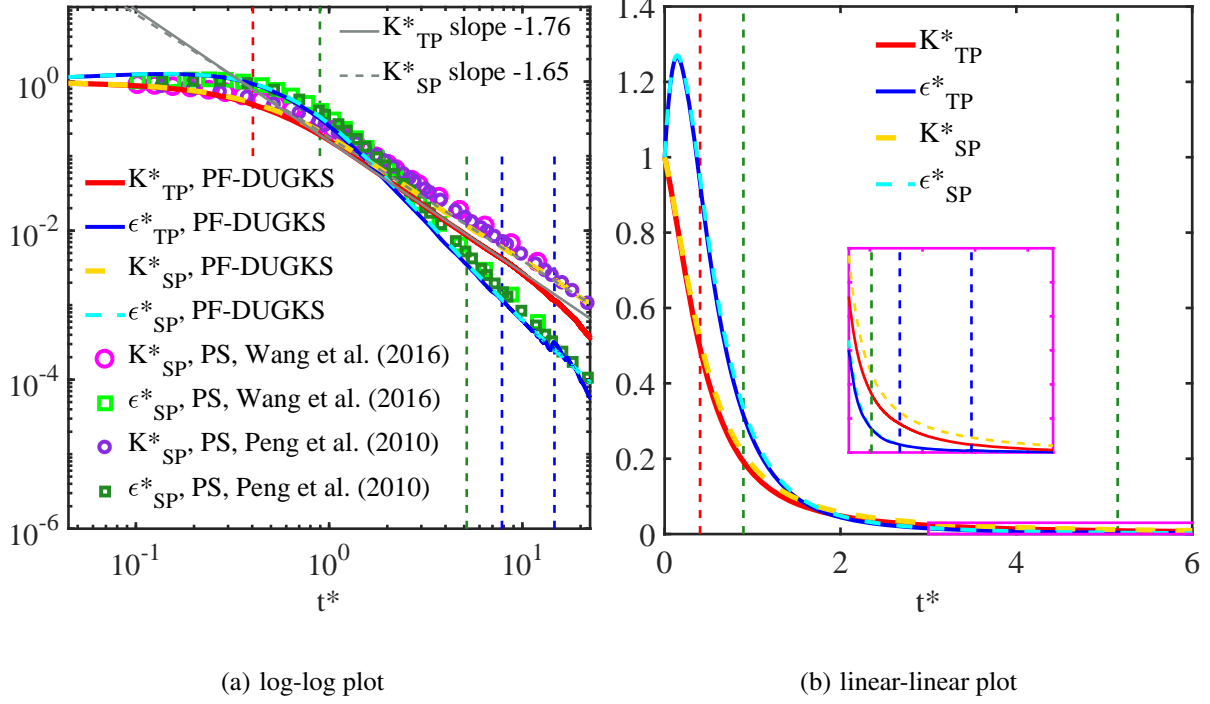


FIG. 19. Evolution of the normalized total kinetic energy $K^* = K(t)/K(0)$ and the normalized dissipation rate $\epsilon^* = \epsilon(t)/\epsilon(0)$. The solid lines represent results from the two-phase (TP) flow and the dashed lines represent those from the single-phase (SP) flow: (a) log-log plot, (b) linear-linear plot. The inset in (b) shows the region $[3, 22.4] \times [0, 0.03]$. The red, dark green, blue vertical dash lines mark typical times for deformation ($t^* = 0.403$), breakup ($t^* = 0.896$ and 5.15), restoration ($t^* = 7.84$ and 14.6), respectively. The resolutions are the same (256^3) for our simulations and Wang's simulation,⁴² while the resolution is lower (128^3) for Peng's simulation.⁷⁷ The initial Re_λ is about 58, 26, 24 for our simulations, Wang's simulations, and Peng's simulations, respectively.

previous studies are also added for comparison. The slopes of our single-phase DHIT results are in good agreement with the those from the PS method reported by Wang *et al.* (2016)⁴² and Peng *et al.* (2010).⁷⁷ Our results cannot overlap with their results precisely for two reasons. First, Re_λ are different, the initial Re_λ is about 58, 26, 24 for our simulation, Wang's simulation, and Peng's simulation, respectively. Huang & Leonard (1994)⁸³ reported that the power-law decay slope of the kinetic energy depends on Re_λ . Second, the decay slope may depend on the shape of the initial energy spectrum used and how the flow is initialized.^{83,84}

Next, we compare our two-phase results with our single-phase results in log-log plot (Fig. 19(a)) and linear-linear plot (Fig. 19(b)). Two general observations can be made. First, the increasing

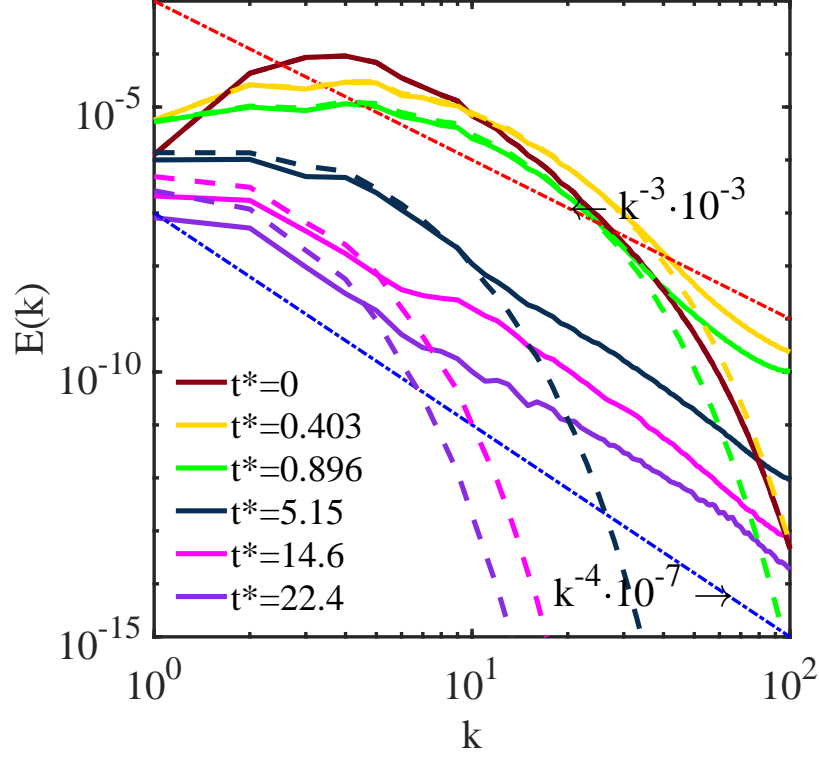


FIG. 20. The energy spectra $E(k, t)$ at different normalized times. The solid lines represent results from the two-phase flow and the dashed lines represent those from the single-phase flow.

fluid-fluid interface area causes the kinetic energy for the two-phase case to decay faster, due to conversion of kinetic energy into the free energy at the deformation stage. The power-law slopes of the kinetic energy decay at the intermediate times (from $t^* = 0.896$ to $t^* = 7.84$ in our simulation) are -1.76 and -1.65 for the two-phase and single-phase flow, respectively. Second, the decay rate of the overall dissipation rate for the two-phase flow, however, is almost the same as that of the single-phase flow. Since the kinetic energy for the two-phase flow is smaller, the viscous dissipation normalized by u'^3/L_I , (i.e., $\varepsilon L_I/u'^3$) for the two-phase flow is then larger, here $L_I = \pi / (2u'^2) \int E(k) / k dk$ is the integral length scale, meaning that the interface boundary layers tend to increase the overall viscous dissipation. However, the coalescence of droplets at the restoration stage would cause transfer of free energy back to kinetic energy, which may also affect the overall viscous dissipation rate. Because the kinetic energy and dissipation rate at that stage are so small (less than 1% of those at the initial time), perturbations due to merging of droplets may affect their value. For example, the dissipation rate fluctuates around $t^* = 14.6$ (see Fig. 19(a)), which could be due to the coalescence of two medium-size droplets at that time (see Fig. 11(k)).

The energy spectrum $E(k, t)$ is also evaluated to show the energy distribution over different

turbulence scales (see Fig. 20). At a given time $t^* > 0$, the energy contained in high wavenumbers for the two-phase flow is larger than the corresponding part in the single-phase flow, while the energy contained in small wavenumbers of two-phase flow is less than the corresponding part in the single-phase flow. This implies that energy is redistributed among scales due to the presence of interfaces, enhancing the transfer of energy from large to small scales. Because the interfaces bring in new intermediate length scales which could increase the transfer rate of energy from low to high wavenumbers.^{11,85} Another reason is that, surface tension force is relatively concentrated around the thin interface, locally similar to the Delta function, and acts as a driving mechanism for small-scale fluctuations when the interface is deformed.

In two-phase flows containing dispersed particles and bubbles, it is well known that the energy spectrum at high wavenumber exhibits a power-law behavior due to wake flows around dispersed objects, different from the exponential decay known for a single-phase turbulence. In the pioneering work of Lance and Bataille (1991),⁸⁶ it was estimated theoretically that dispersed wakes due to bubbles can produce a power-law of slope approximately equal to -3 based on the experimental data. The bubbly-flow simulation results of Bunner and Tryggvason (2002)⁸⁷ suggested a power slope of -3.6 at high wavenumbers, where they applied the front-tracking/finite difference method and did not allow the bubbles to coalesce. In a study of freely-decaying turbulence containing breakup of a liquid sheet applying level-set method, Trontin *et al.* (2010)⁸⁸ found a power-law of slope between -3 and -5 within the breakup region.

In Fig. 20, we also clearly observe power-law spectra at high wavenumbers, with a slope approximately equal to -4 . The governing equation of $E(k, t)$ is derived in Appendix C 1, which shows that there is a new term, $S(k, t)$, due to the surface tension effect. This term could act to transfer the kinetic energy from low wavenumbers to high wavenumbers.

F. Kinetic energy spectra on spheres and velocity field inside/outside the droplets

Since the initial setting of the physical problem is also approximately spherically symmetric, we also show the kinetic energy on the spheres with different radii from the center of the system in Fig. 21, to examine the energy distribution at different scales on the surfaces of spheres. The corresponding velocity fields are shown in Fig. 22. The effects of the fluid-fluid interfaces could be more clearly shown, particularly during the deformation stage. The main influencing factors here are the relative volume fractions of the two phases and the distribution of the fluid-fluid interface,

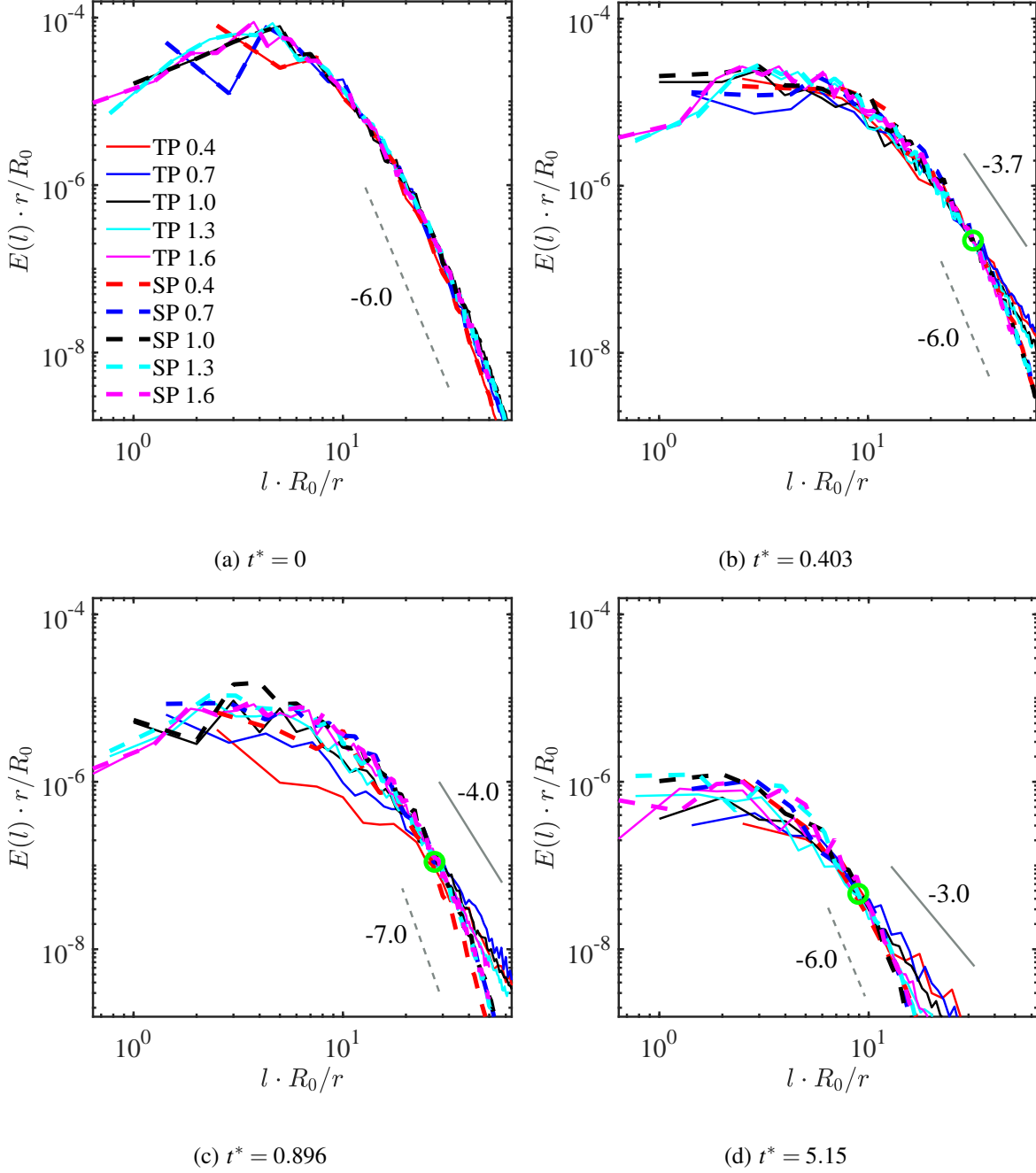


FIG. 21. Energy spectra based on the spherical harmonics at different times for the two-phase flow and the single-phase flow, at different radii, $r/R_0 = 0.4, 0.7, 1.0, 1.3, 1.6$, from the initial droplet center. The solid lines represent results for the two-phase (TP) flow and the dashed lines for the single-phase (SP) flow. The green circles in (b), (c) and (d) indicate the approximate cross-over location, where the relative magnitudes of the TP energy spectra change from below to above those of the SP flow.

at different distances from the center of the initial droplet.

At $t^* = 0$ (Fig. 21(a)), the kinetic energy spectra on different spherical surfaces almost overlap one another at large wavenumbers, because the initial turbulent flow field is homogeneous and isotropic. Furthermore, the energy spectra of two-phase flow and single-phase flow are exactly the same at this time, because of the same initial velocity field, as shown in Fig. 22(a)) and Fig. 22(e)).

At an early time $t^* = 0.403$, turbulence distorts the interface significantly while the interfaces slightly weaken the nearby velocity magnitude (Fig. 22(b)), compared to the corresponding regions of single-phase flow (Fig. 22(f)). Compared to Fig. 21(a), Fig. 21(b) shows that the kinetic energies decay in the large scales, while increase in the small scales. The kinetic energies of two-phase flow are smaller than those of single-phase flow in large scales, but larger in small scales. The reasons are the same as those for Fig. 20. The main difference of Fourier expansion and spherical harmonics expansion is that, Fig. 20 is the expansion in the whole simulation region, while Fig. 21 is the expansion on the specific spherical surfaces. As a result, the kinetic energy in Fig. 20 can be viewed closed, which cannot transfer to other space, since the boundary conditions are periodic. But the kinetic energy in Fig. 21 is open, it can transfer from one spherical surface to other spherical surfaces. However, the energy spectra for spherical harmonics and Fourier appear to be similar.

When $t^* = 0.896$ (Fig. 21(c)), the general shape of spherical harmonics spectra are similar to those at $t^* = 0.403$. However, the effect of droplets on the velocity magnitude field becomes significant at this time. The velocity magnitude inside the droplet is less than that outside the droplet (see Fig. 22(c)), and it is also less than that in the corresponding regions of single-phase flow field (compared to Fig. 22(g)). Because there is a deformed droplet at the center of the computational domain at this time, it appears that the fluid-fluid interface or surface tension force limits the movement of the fluid inside the droplet, reducing the flow velocity fluctuations and kinetic energy. Scarbolo & Soldati (2013)¹⁹ also drew a similar conclusion, that the velocity magnitude is damped inside the droplet in a turbulent channel flow simulation. Outside the droplets, the velocity magnitude contour of two-phase flow is still similar to that of single-phase flow, because a large volume fraction of the bulk region is away from the interface. From the point of view of spherical harmonics spectra, the large scale two-phase kinetic energy on the small spherical surface $r = 0.4R_0$ is much less than that on the larger spherical surfaces, and single-phase $r = 0.4R_0$ sphere, as shown in Fig. 21(c).

At $t^* = 5.15$ (see Fig. 22(d) and Fig. 22(h)), the velocity magnitude inside the droplets remains smaller, but not as obvious as before, since the velocity magnitude is small in the whole flow field

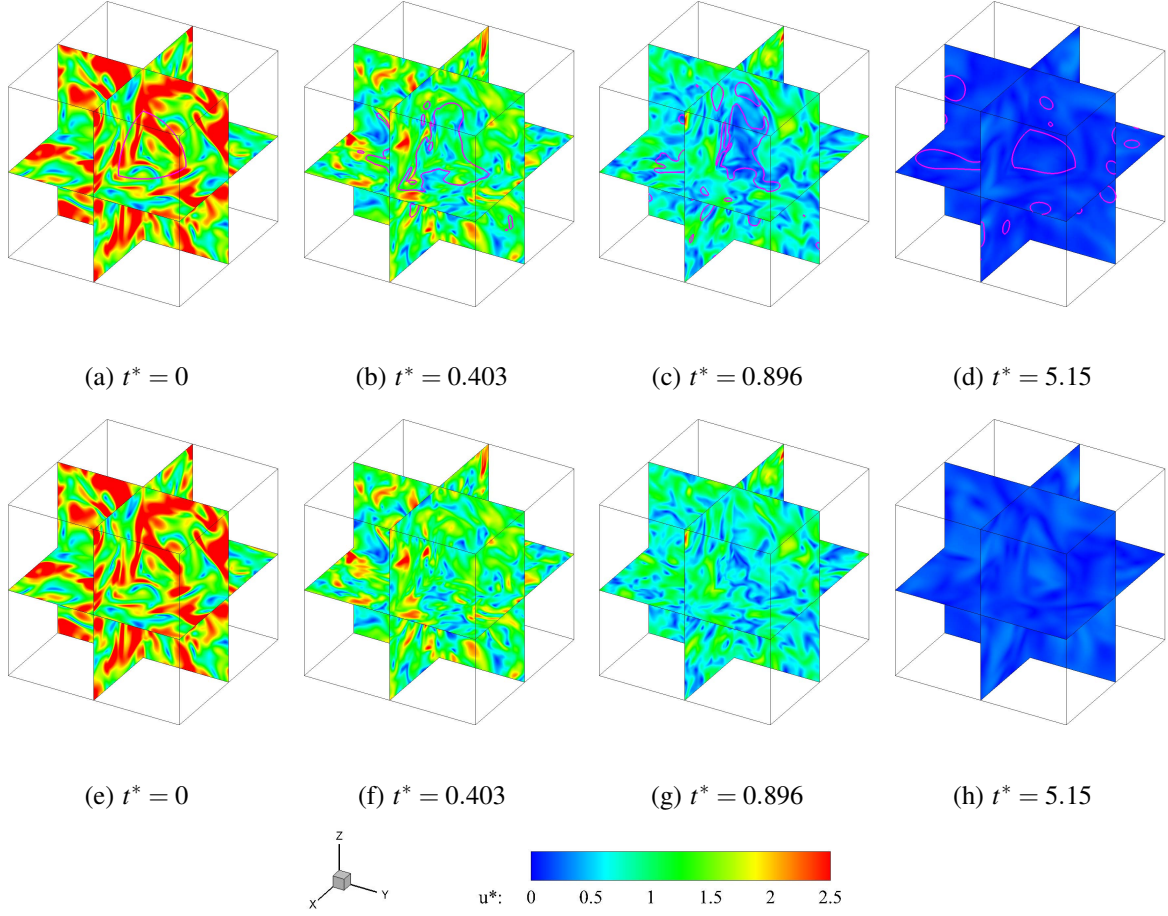


FIG. 22. Velocity magnitude $u^* = |\mathbf{u}| / [u'(t^* = 0)]$ on the central planes in the three directions at different times. The first row is for the two-phase flow and the second row for the single-phase flow. The purple lines in the first row are the intersecting lines between fluid-fluid interface $\phi = 0.5$ and the central planes.

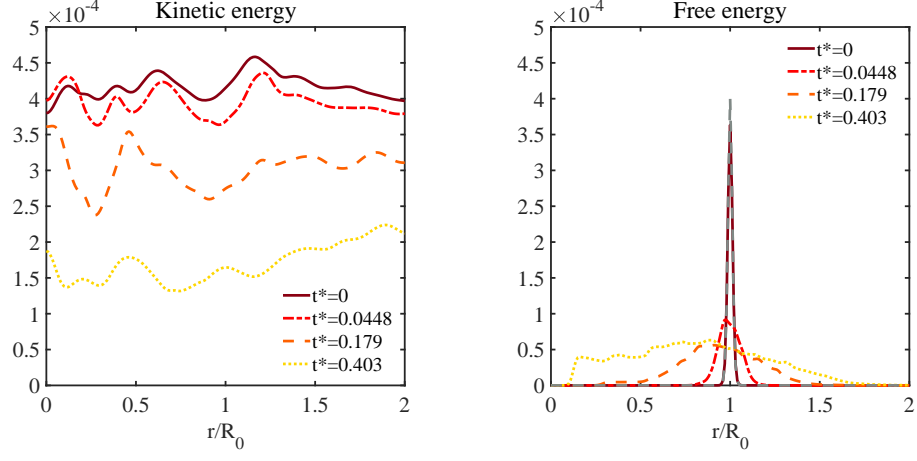
for the later period of DHIT. Furthermore, the velocity magnitude outside the droplets are smaller than that in the single-phase flow, because the stored interface energy by small daughter droplets could not return fully back to the kinetic energy, even at this late time. The spherical harmonics spectra also shows the same results (Fig. 21(d)).

Quantitatively, the slopes in the high wavenumber range of kinetic energy in the spherical harmonics spaces are usually about -6 for single-phase flow, while the values are between -4 and -3 for the two-phase flow, which are similar to that in the Fourier spectra in Fig. 20.

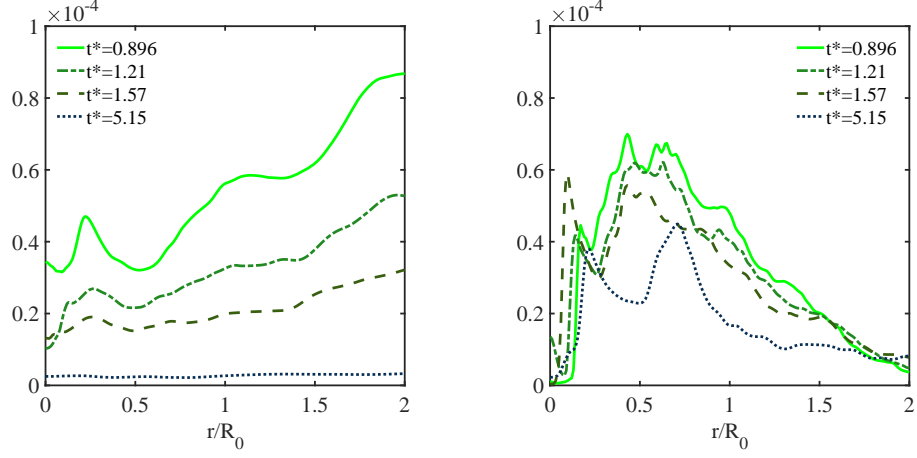
G. Interaction between kinetic energy and free energy

To explicitly demonstrate the exchange between kinetic energy and free energy, Fig. 23 shows the spherical averaged kinetic energy and free energy as a function of distance from the initial droplet center, at different times during the three stages. At $t^* = 0$, the magnitude of free energy near the interface is close to kinetic energy because of the parameters setting, while it is negligible away from the interface. The averaged kinetic energy is almost independent of the radial distance from the center, because of the homogeneous isotropic flow initialization. Therefore, the kinetic energy is much larger than the free energy in the integral sense at the initial time. As time proceeds, the kinetic energy decays because of the viscous dissipation and the increasing free energy, while the free energy spreads over a larger region because of the droplet deformation. The total kinetic energy is still much larger than the free energy during the deformation stage, as shown in Fig. 23(a). During the breakup stage (Fig. 23(b)), the kinetic energy has decreased to a magnitude which is comparable to the free energy. At the restoration stage (Fig. 23(c)), the kinetic energy is much less than the free energy, only about 1% of the latter. The above analysis, again, illustrates that (a) during the deformation stage, kinetic energy plays a dominant role on the interface evolution with the free energy rapidly increasing at the cost of the kinetic energy, (b) during the breakup stage, kinetic energy and free energy are interchanged and comparable, and (c) the free energy plays a dominant role during the restoration stage. As shown in Fig. 11, most of the interface region is close to the center of the computational domain. Therefore, at the restoration stage (see Fig. 23(c)), the free energy is concentrated near the center, resulting in a small kinetic energy near the center partially due to the exchange between the two energy forms.

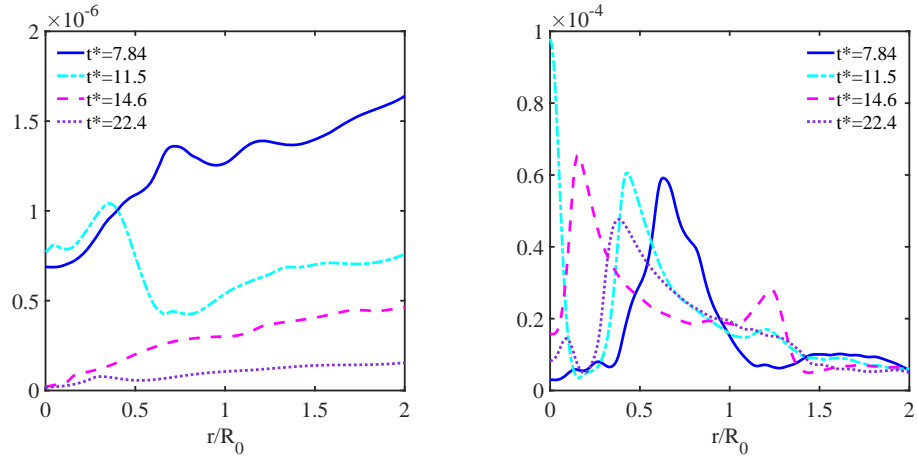
The total kinetic energy and free energy as a function of time are shown in Fig. 24. Again, the results demonstrate that the total kinetic energy is much larger than the total free energy during the deformation stage, becomes comparable to the total free energy during the breakup stage, and falls off to a value much smaller than the total free energy during the restoration stage. The total interface area and total free energy increases rapidly during the deformation stage, by a factor of about 5, then decreases slowly with time afterwards.



(a) Deformation stage



(b) Breakup stage



(c) Restoration stage

FIG. 23. Spherically averaged energies as a function of radial distance from the initial droplet center at different times. The gray dashed line in (a) is the analytical result of free energy at the initial time based on Eq. (31).

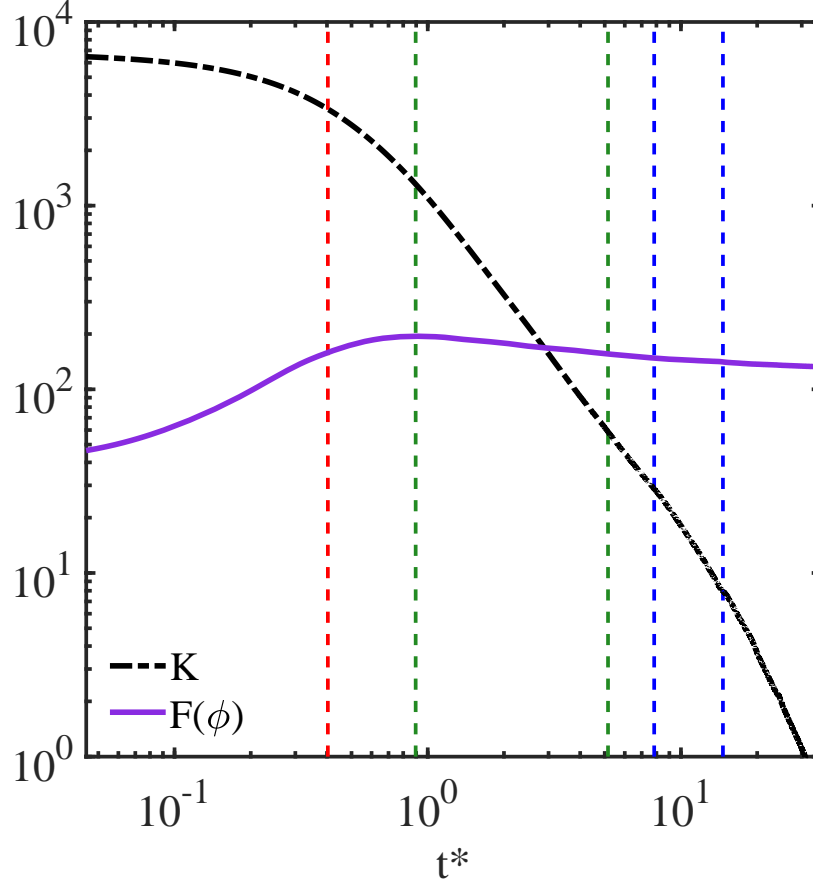


FIG. 24. Time evolution of the overall kinetic energy and free energy. The vertical dashed lines from left to right mark $t^*=0.403, 0.896, 5.15, 7.84, 14.6$, respectively.

VI. CONCLUSIONS

A three-dimensional (3D) direct numerical simulation (DNS) code is developed to simulate immiscible two-phase turbulent flows based on the PF-DUGKS approach. This approach solves equivalently the Cahn-Hilliard-Navier-Stokes (CHNS) system by the use of two Boltzmann equations. After a stationary droplet and a freely-deforming droplet in a turbulent background flow were simulated to test the PF-DUGKS code, we focused on applying the approach to study the breakup process of a large spherical droplet in a DHIT background flow. The breakup process was observed to consist of three distinct stages. The results for the two-phase flow simulations are compared with those of the single-phase ($\phi = 0$) decaying turbulence using the same code. The comparisons indicate that the phase-field approach can be coupled with DUGKS to simulate three-dimensional immiscible two-phase turbulent flows. Main results are summarized as follows.

A 3D static droplet is simulated to show that the kinetic energy in the spurious currents are

negligibly small when compared to the free energy. In the case of a freely-deforming droplet (*i.e.*, with negligible surface tension effects) in decaying turbulence, the kinetic energy spectra on spherical surfaces based on the two-phase setting (with a negligible surface tension) are compared with those based on the single-phase setting ($\phi = 0, \sigma \sim O(10^{-3})$). The comparisons show that the two limiting approaches yield the same results, implying that (1) the two-phase flow at very large We number ($\sim O(10^{17})$) is similar to the single-phase flow because the effect of surface tension on the flow field is essentially removed, (2) the use of a constant order parameter $\phi = 0$ in the whole flow field naturally reduces the solved system to a single-phase flow. Furthermore, our results demonstrate that the spherical harmonics can help understand the simultaneous energy transfer process along the radial direction and across different length scales, taking advantage of the fact that the chosen physical problem is spherically symmetric.

The breakup of a large spherical droplet in DHIT is the main focus of this study, thus we provide an in-depth analysis of the numerical results from several different angles. The main parameters we used are as follows: density ratio and viscosity ratio are both set to one, the dispersed phase volume fraction ϕ is 6.54%, the initial Weber number We is 21.7, and the initial Taylor microscale Reynolds number Re_λ is 58. The simulation results show that the breakup of a spherical droplet in DHIT can be separated into three stages, namely, the deformation stage, the breakup stage and the restoration stage. It is shown that the dividing time between the breakup stage and the restoration stage can be roughly described by the Hinze criterion. The deformation stage takes the shortest time, while the restoration stage takes the longest time.

During the deformation stage, the initial spherical droplet wrinkles and elongates in every direction. The droplet interface becomes bumpy and the interface curvature increases. The total interface area is increased by a factor larger than 4 at the end of this first stage. The kinetic energy is larger than free energy at this stage, and plays a dominant role, which can be also interpreted by the value of Weber number ($We \gg 1$).

During the breakup stage, the droplet continues to stretch and break, forming a large numbers of daughter droplets (about 60 in the end of this stage) of different sizes. Roughly, over 60% of droplets in number are with a diameter less than $0.1D_0$. The total interface area becomes larger due to droplet breakup, but at the same time is reduced due to the tendency for daughter droplets to restore the spherical shape. The overall trend of interface area in the breakup stage is a reduction of the interface area. The Weber number at this stage is of the order one. The kinetic energy and free energy are interchanged and comparable during this stage, and they influence the evolution of

droplets, together.

During the restoration stage, all the droplets relax towards spherical shape. Therefore, the total area decreases. Occasionally two droplets close to each other could coalesce, disturbing the nearby flow field and the total area. It is shown that $We \ll 1$ at the stage. The restoration stage is mainly driven by surface tension force, since the kinetic energy is very small compared to the free energy.

Since the droplet is initialized in the center of the box, the free energy is distributed around the center in the whole evolution period. Although the kinetic energy is homogeneous isotropic at the beginning, its distribution can become distance-dependent, due to the reduction of velocity field by fluid-fluid interface or by surface tension force, or the conversion from kinetic energy to free energy. For the same reason, the velocity magnitude near the interface is attenuated during the whole evolution. However, the vorticity magnitude field near the interface is argued, since the fluid-fluid interface boundary layer could generate vorticity.

The power-law decay of the two-phase kinetic energy at the breakup stage has an exponent 1.76, while it is 1.65 for single-phase flow during the same time, as a part of the kinetic energy is converted to free energy for the two-phase flow. In the spherical harmonics space, the power-law slopes in the high wavenumber region are usually about -6 for single-phase flow, while the values are between -4 and -3 for two-phase flow, which are similar to the power-law slope in the Fourier spectra.

The study of interface evolution in immiscible fluids, in particular under more general conditions (*e.g.*, higher density ratio), is relevant to the atomization process.^{89,90} These general conditions under the PF-DUGKS approach have been addressed by combining with conservative Allen-Cahn equation.^{91,92} Their applications to three-dimensional complex two-phase flows will be a subject of further investigation.

ACKNOWLEDGMENTS

This work has been supported by the National Numerical Wind Tunnel program, the Taizhou-Shenzhen Innovation Center, the National Natural Science Foundation of China (NSFC award numbers 91852205, 91741101 & 11961131006), NSFC Basic Science Center Program (Award number 11988102), Guangdong Provincial Key Laboratory of Turbulence Research and Applications (2019B21203001), Guangdong-Hong Kong-Macao Joint Laboratory for Data-Driven Fluid Mechanics and Engineering Applications (2020B1212030001) and Shenzhen Science and Tech-

nology Program (Grant No. KQTD20180411143441009). Computing resources are provided by the Center for Computational Science and Engineering of Southern University of Science and Technology. The authors also wish to thank Dr. Chéron Victor P. Gerard, Mr. Zelong Yuan, and Mr. Mingyu Su for helpful discussions.

Appendix A: Inverse design of the model Boltzmann equations for the CHNS system based on the Chapman-Enskog analysis

The purpose of this appendix is to derive all the moment-integral constraints for f^{eq} , g^{eq} , S_α^f , and S_α^g in Eqs. (8a-b), in order to reproduce the CHNS system, Eqs. (6a-c). Two model Boltzmann equations, *i.e.*, Eqs. (8a-b), are introduced, with f representing the pressure/velocity distribution function and g the order-parameter distribution function, *i.e.*,

$$p = \int f d\xi, \quad RT\rho u_j = \int f \xi_j d\xi, \quad \phi = \int g d\xi. \quad (\text{A1})$$

As noted previously, the pressure p and density ρ are independent. The density field ρ is solely determined by the phase field ϕ according to Eq. (7a). Since p and u_j share the same distribution f , thus $\rho RT u_j$ is viewed as the first moment of f . The equilibrium f^{eq} is designed by modifying the standard Maxwellian distribution, under the Hermite expansion, as

$$f^{eq} = w(\xi) \left[p + \rho RT \left(\frac{\xi \cdot \mathbf{u}}{RT} + \frac{1}{2} \frac{(\xi \cdot \mathbf{u})^2}{(RT)^2} - \frac{1}{2} \frac{u^2}{RT} + \mathcal{O}(Ma^3) \right) \right], \quad (\text{A2})$$

where

$$w(\xi) \equiv \frac{1}{(2\pi RT)^{D/2}} \exp\left(-\frac{\xi^2}{2RT}\right). \quad (\text{A3})$$

It follows that

$$\int f^{eq} d\xi = p, \quad (\text{A4a})$$

$$\int f^{eq} \xi_j d\xi = RT\rho u_j, \quad (\text{A4b})$$

$$\int \xi_j \xi_m f^{eq} d\xi = RT (\rho u_j u_m + p \delta_{jm}), \quad (\text{A4c})$$

$$\int \xi_j \xi_m \xi_n f^{eq} d\xi = \rho (RT)^2 (u_j \delta_{mn} + u_m \delta_{jn} + u_n \delta_{mj}). \quad (\text{A4d})$$

It is noted that the above Hermite expansion is consistent with the D3Q19 lattice velocity model used in this paper.

Eqs. (A4a) and (A4b) imply the collision term in Eq. (8a) makes no contribution to the zeroth-order and first-order moment equations. Similarly, we require that the collision term in Eq. (8b) conserves the phase field by setting

$$\int g^{eq} d\xi = \phi. \quad (\text{A5})$$

The continuity equation is derived from the zeroth-order moment of Eq. (8a), *i.e.*,

$$\int \left[\frac{\partial f}{\partial t} + \xi_m \frac{\partial f}{\partial x_m} = -\frac{f - f^{eq}}{\tau_f} + S^f \right] d\xi. \quad (\text{A6})$$

Substituting Eq. (A1), Eq. (A5) into Eq. (A6), yields

$$\frac{\partial p}{\partial t} + \frac{\partial}{\partial x_m} (RT \rho u_m) = 0 + \int S^f d\xi. \quad (\text{A7})$$

Comparing this to the continuity equation Eq. (6a), we need to set the zeroth-order moment of S^f to

$$\int S^f d\xi = RT \left[u_m \frac{\partial \rho}{\partial x_m} - \rho \gamma \frac{\partial}{\partial x_m} \left(M_{CH} \frac{\partial \mu_\phi}{\partial x_m} \right) \right]. \quad (\text{A8})$$

To proceed further, we introduce the Chapman-Enskog expansion of the distribution functions

$$f = f^{eq} - \tau_f \left(\frac{\partial f^{eq}}{\partial t} + \xi_j \frac{\partial f^{eq}}{\partial x_j} - S^f \right) + \mathcal{O}(\tau_f^2), \quad (\text{A9a})$$

$$g = g^{eq} - \tau_g \left(\frac{\partial g^{eq}}{\partial t} + \xi_j \frac{\partial g^{eq}}{\partial x_j} - S^g \right) + \mathcal{O}(\tau_g^2). \quad (\text{A9b})$$

Note that the continuity equation remains the same at the different orders in the Chapman-Enskog expansion.

To the leading order, the first-order moment equation of Eq. (8a) and the zeroth-order moment equations of Eq. (8b) yield

$$RT \frac{\partial(\rho u_j)}{\partial t} + RT \frac{\partial(\rho u_m u_j + p \delta_{mj})}{\partial x_m} = 0 + \int S^f \xi_j d\xi + \mathcal{O}(\tau_f), \quad (\text{A10a})$$

$$\frac{\partial \phi}{\partial t} + \frac{\partial}{\partial x_m} \int \xi_m g^{eq} d\xi = \int S^g d\xi + \mathcal{O}(\tau_g). \quad (\text{A10b})$$

These two equations should reproduce the momentum equation and the CH equation to the same leading order, namely, without the diffusion terms. A convenient choice for the three involved moments is

$$\int S^f \xi_j d\xi = RT F_j, \quad (\text{A11a})$$

$$\int \xi_m g^{eq} d\xi = \phi u_m, \quad (\text{A11b})$$

$$\int S^g d\xi = 0. \quad (\text{A11c})$$

The leading-order equations, Eqs. (6a) (A10a) (A10b), together with Eq. (7a), allow us to express all the time derivatives, to the leading-order, as

$$\frac{\partial \phi}{\partial t} = -\frac{\partial}{\partial x_m} (\phi u_m) + \mathcal{O}(\tau_g), \quad (\text{A12a})$$

$$\frac{\partial \rho}{\partial t} = -\frac{\partial}{\partial x_m} (\rho u_m) + \frac{(\rho_A - \rho_B)}{(\phi_A - \phi_B)} \frac{1}{\gamma} \frac{\partial u_m}{\partial x_m} + \mathcal{O}(\tau_g), \quad (\text{A12b})$$

$$\frac{\partial p}{\partial t} = -\rho RT \frac{\partial u_m}{\partial x_m} - \rho RT \gamma \frac{\partial}{\partial x_m} \left(M_{CH} \frac{\partial \mu_\phi}{\partial x_m} \right), \quad (\text{A12c})$$

$$\frac{\partial u_j}{\partial t} = -u_m \frac{\partial u_j}{\partial x_m} - \frac{(\rho_A - \rho_B) u_j}{(\phi_A - \phi_B) \gamma \rho} \frac{\partial u_m}{\partial x_m} - \frac{1}{\rho} \frac{\partial p}{\partial x_j} + \frac{F_j}{\rho} + \mathcal{O}(\tau_f) + \mathcal{O}(\tau_g Ma). \quad (\text{A12d})$$

where $Ma = U/\sqrt{RT}$ denotes the Mach number with U being the velocity scale.

Now we proceed to keep the $\mathcal{O}(\tau_f, \tau_g)$ terms. According to Eq. (A9a), the momentum equation becomes

$$\begin{aligned} & \frac{\partial}{\partial t} (\rho u_j) + \frac{\partial (\rho u_j u_m)}{\partial x_m} \\ &= -\frac{\partial p}{\partial x_j} + F_j + \frac{1}{RT} \frac{\partial}{\partial x_m} \tau_f \int \left(\frac{\partial f^{eq}}{\partial t} + \xi_n \frac{\partial f^{eq}}{\partial x_n} - S^f \right) \xi_m \xi_j d\xi + \mathcal{O}(\tau_f^2), \end{aligned} \quad (\text{A13})$$

where the $\mathcal{O}(\tau_f)$ term should approximate the viscous term, *i.e.*,

$$\tau_f \int \left(\frac{\partial f^{eq}}{\partial t} + \xi_n \frac{\partial f^{eq}}{\partial x_n} - S^f \right) \xi_m \xi_j d\xi = RT \mu \left(\frac{\partial u_j}{\partial x_m} + \frac{\partial u_m}{\partial x_j} \right) + \mathcal{O}(\tau_f^2), \quad (\text{A14})$$

where $\mu = \rho RT \tau_f$.

Using Eqs. (A12b-d) and Eq. (A14), we can obtain

$$\begin{aligned} & \tau_f \int S^f \xi_m \xi_j d\xi \\ &= \tau_f \left[\frac{\partial}{\partial t} \int f^{eq} \xi_j \xi_m d\xi + \frac{\partial}{\partial x_n} \int f^{eq} \xi_j \xi_m \xi_n d\xi \right] - RT \mu \left(\frac{\partial u_j}{\partial x_m} + \frac{\partial u_m}{\partial x_j} \right) \\ &= \tau_f RT \left[\frac{\partial}{\partial t} (\rho u_m u_j + p \delta_{mj}) + RT \frac{\partial}{\partial x_n} (\rho u_j \delta_{mn} + \rho u_m \delta_{jn} + \rho u_n \delta_{mj}) \right] \\ &= \tau_f RT \left\{ u_j F_m + u_m F_j + RT \left(u_n \frac{\partial \rho}{\partial x_n} \delta_{mj} + u_j \frac{\partial \rho}{\partial x_m} + u_m \frac{\partial \rho}{\partial x_j} \right) - RT \rho \gamma \frac{\partial}{\partial x_n} \left(M_{CH} \frac{\partial \mu_\phi}{\partial x_n} \right) \delta_{mj} \right\} \\ & \quad + \mathcal{O}(\tau_f^2, \tau_f \tau_g Ma^2, \tau_f Ma^3). \end{aligned} \quad (\text{A15})$$

Namely, the requirement for the second-order moment of S^f is

$$\begin{aligned} \int S^f \xi_m \xi_j d\xi &= RT [u_j F_m + u_m F_j] \\ &+ (RT)^2 \left[u_n \frac{\partial \rho}{\partial x_n} \delta_{mj} + u_j \frac{\partial \rho}{\partial x_m} + u_m \frac{\partial \rho}{\partial x_j} - \rho \gamma \frac{\partial}{\partial x_n} \left(M_{CH} \frac{\partial \mu_\phi}{\partial x_n} \right) \delta_{mj} \right]. \end{aligned} \quad (A16)$$

Similarly, by retaining the $\mathcal{O}(\tau_g)$ terms in the zeroth-order moment of Eq. (8b), we have

$$\frac{\partial \phi}{\partial t} + \frac{\partial(\phi u_m)}{\partial x_m} = \frac{\partial}{\partial x_m} \left[\tau_g \int \left(\frac{\partial g^{eq}}{\partial t} + \xi_j \frac{\partial g^{eq}}{\partial x_j} - S^g \right) \xi_m d\xi \right] + \mathcal{O}(\tau_g^2). \quad (A17)$$

By matching the first-order term with the diffusion term in the CH equation, we have

$$\begin{aligned} \tau_g \int S^g \xi_j d\xi &= \tau_g \left[\frac{\partial}{\partial t} \int g^{eq} \xi_j d\xi + \frac{\partial}{\partial x_m} \int g^{eq} \xi_m \xi_j d\xi \right] - M_{CH} \frac{\partial \mu_\phi}{\partial x_j} + \mathcal{O}(\tau_g^2) \\ &= \tau_g \left[\frac{\partial}{\partial t} (\phi u_j) + \frac{\partial}{\partial x_m} \int g^{eq} \xi_m \xi_j d\xi \right] - M_{CH} \frac{\partial \mu_\phi}{\partial x_j} + \mathcal{O}(\tau_g^2), \end{aligned} \quad (A18)$$

where $M_{CH} = \tau_g \eta RT$. From Eqs. (A12a) and (A12d), the time derivative term can be expressed as

$$\frac{\partial}{\partial t} (\phi u_j) = -\frac{\partial}{\partial x_m} (\phi u_m u_j) + \frac{\phi}{\rho} \left(F_j - \frac{\partial p}{\partial x_j} \right) + \mathcal{O}(\tau_g, \tau_f, Ma^3). \quad (A19)$$

Then

$$\begin{aligned} \tau_g \int S^g \xi_j d\xi &= \tau_g \frac{\partial}{\partial x_m} \left(\int g^{eq} \xi_m \xi_j d\xi - \phi u_m u_j - \eta RT \mu_\phi \delta_{mj} \right) + \tau_g \frac{\phi}{\rho} \left(F_j - \frac{\partial p}{\partial x_j} \right) \\ &+ \mathcal{O}(\tau_g^2, \tau_f \tau_g, \tau_g Ma^3). \end{aligned} \quad (A20)$$

Since two moments can be assigned, the most convenient choice would be

$$\int g^{eq} \xi_m \xi_j d\xi = \phi u_m u_j + \eta RT \mu_\phi \delta_{mj}, \quad (A21a)$$

$$\int S^g \xi_j d\xi = \frac{\phi}{\rho} \left(F_j - \frac{\partial p}{\partial x_j} \right). \quad (A21b)$$

To summarize, the integral constraints for the model Boltzmann equations, Eqs. (8a) and (8b), include:

1. The continuity equation sets the zeroth-order moment for S^f , Eq. (A8);
2. The momentum equation provides the first-order and second-order moments for S^f , Eq. (A11a), and Eq. (A16);
3. The CH equation leads to the first- and second-order moments of g^{eq} , Eqs. (A11b) and (A21a), and the zeroth- and first-order moments for S^g , Eqs. (A11c) and (A21b).

The above analyses have outlined that the moments up to the third order for f^{eq} , up to the second order for g^{eq} and S^f , and up to the first order for S^g are involved in the inverse design. Rigorously speaking, a Gauss-Hermite quadrature of a sixth order is needed for f , and a Gauss-Hermite quadrature of a fourth order is needed for g . The D3Q19 lattice velocity model provides only a fifth-order Gauss-Hermite quadrature, which is the reason that we require the $\mathcal{O}(Ma^3)$ terms must be negligible.

We emphasize that the above integral conditions are designed as a convenient choice, but not the only choice. In other words, they represent a set of sufficient conditions, not the necessary conditions. For example, one equation, Eq. (A20), is used to assign two conditions, Eqs. (A21a) and (A21b), there are many possibilities.

Furthermore, even with the convenient design stated by the above integral constraints, there are many ways to specify the precise forms for g^{eq} , S^f , and S^g . We can confirm that the specific forms given in Eqs. (11) and (13) do meet all the requirements stated above. We can also introduce other specific forms, for example, utilizing the Hermite expansion formulae, as done in^{93,94}. Since the stability and accuracy of the forms in Eqs. (11) and (13) have been verified by the previous studies,^{45,46} we apply them for the droplet breakup simulation here.

Appendix B: The algorithm for computing the volume of individual droplets

During the breakup process, we wish to identify individual droplets and compute their volumes. We developed an algorithm for this purpose. In this appendix, we briefly describe the algorithm to isolate the region for an individual droplet. Here an individual droplet is defined as a set of connected nodes with $\phi \geq 0.5$. Two nodes with $\phi \geq 0.5$ are viewed to be associated with a same droplet if they are connected by a set of nodes with $\phi \geq 0.5$.

The procedure is as follows:

1. Simplify the field data. All nodes with $\phi \geq 0.5$ are reassigned a value of $\phi = 1$, and all with $\phi < 0.5$ are set to $\phi = 0$. After this procedure, $\phi = 1$ represents the droplet phase (the dispersed phase), while $\phi = 0$ represents the background phase (the continuous phase).
2. Find and mark the seed position for one droplet. We first find a node location (i_0, j_0, k_0) with $\phi = 1$, which means that there is a droplet around (i_0, j_0, k_0) . Then we change the ϕ value from 1 to 50 for this specific position, *i.e.*, $\phi(i_0, j_0, k_0) = 50$. The reason why we set

$\phi(i_0, j_0, k_0) = 50$ is to isolate it and other connected droplet nodes from the un-connected droplet nodes with $\phi = 1$. In fact, we only need a value larger than 27 ($= 3^3$), and 50 is a convenient choice. We refer to this location as the seed position for the current droplet.

3. Find all the droplet node points connected to (i_0, j_0, k_0) . We then check the immediate neighborhood, *i.e.*, the $\phi(i, j, k)$ values for nodes $i_0 - 1 \leq i \leq i_0 + 1, j_0 - 1 \leq j \leq j_0 + 1, k_0 - 1 \leq k \leq k_0 + 1$. If any of these points is outside the computational domain, then periodic boundary condition is employed to provide the ϕ value. If $\phi(i, j, k) = 1$ is found in this region, *i.e.*, $\phi(i_1, j_1, k_1) = 1$, then compute the sum $\sum \phi(i, j, k)$ with $i_1 - 1 \leq i \leq i_1 + 1, j_1 - 1 \leq j \leq j_1 + 1, k_1 - 1 \leq k \leq k_1 + 1$. If this sum is larger than 50, which implies that the two nodes (i_1, j_1, k_1) and (i_0, j_0, k_0) are connected nodes; then $\phi(i_1, j_1, k_1)$ is set to 50. If at least one new connected node is found in this previous search, the process continues to the region $\phi(i, j, k)$ with $i_0 - 2 \leq i \leq i_0 + 2, j_0 - 2 \leq j \leq j_0 + 2, k_0 - 2 \leq k \leq k_0 + 2$, to see if any new connected nodes can be identified. Otherwise, all droplet nodes connected to the seed node (i_0, j_0, k_0) have been found.
4. Calculate the volume of this current droplet. Simply count the number of grid points with $\phi = 50$ encountered in Step 2 and Step 3.
5. Repeat the process to find other droplets. We remove all the node points with $\phi = 50$ by changing the ϕ value to 0 for these nodes. Then go back to Step 2, repeat Steps 2 to 4.

Appendix C: Kinetic energy in the spectral space

We focus on the isothermal two-phase flow with same density and same viscosity for the two phases. The density is ρ_0 , the dynamic viscosity is μ_0 , the kinematic viscosity is ν_0 . It is also assumed that no other forcing term exists.

1. Kinetic energy evolution in the Fourier space

Converting the energy balance evolution into the Fourier space allows us to study the energy transfer across different scales for the multiphase flow system.

Eq. (6b) can be written equivalently as

$$\frac{\partial(\rho u)}{\partial t} + \nabla \cdot (\rho u u) = -\nabla P + \nabla \cdot [\mu (\nabla u + u \nabla)] - \kappa \nabla \cdot (\nabla \phi \nabla \phi), \quad (C1)$$

where $P = p + \phi\mu_\phi - (\psi + \kappa|\nabla\phi|^2/2)$.

Taking the Fourier transform of Eq. (C1) yields the momentum equation in the wavenumber space

$$\begin{aligned} & \left(\frac{\partial}{\partial t} + \nu_0 k^2 \right) \hat{\mathbf{u}}(\mathbf{k}, t) \\ &= \left(\mathbf{I} - \frac{\mathbf{k}\mathbf{k}}{k^2} \right) \cdot \left\{ \begin{aligned} & -\sqrt{-1} \sum_{\mathbf{k}'+\mathbf{k}''=\mathbf{k}} [\mathbf{k} \cdot \hat{\mathbf{u}}(\mathbf{k}', t) \hat{\mathbf{u}}(\mathbf{k}'', t)] \\ & + \frac{\kappa}{\rho_0} \sqrt{-1} \sum_{\mathbf{k}'+\mathbf{k}''=\mathbf{k}} [\mathbf{k} \cdot \mathbf{k}'\mathbf{k}'' \hat{\phi}(\mathbf{k}', t) \hat{\phi}(\mathbf{k}'', t)] \end{aligned} \right\}, \end{aligned} \quad (\text{C2})$$

where \mathbf{k} is the wavenumber, $k = |\mathbf{k}|$ is the magnitude of \mathbf{k} , \mathbf{I} is the second-order unit tensor. $(\mathbf{I} - \mathbf{k}\mathbf{k}/k^2)$ is the projection tensor.

Then the kinetic energy of Fourier mode, $\hat{E}(\mathbf{k}, t) = \hat{\mathbf{u}}_*(\mathbf{k}, t) \cdot \hat{\mathbf{u}}(\mathbf{k}, t) / 2$, is

$$\frac{\partial}{\partial t} \hat{E}(\mathbf{k}, t) = \hat{T}(\mathbf{k}, t) + \hat{S}(\mathbf{k}, t) - 2\nu_0 k^2 \hat{E}(\mathbf{k}, t), \quad (\text{C3})$$

where

$$\begin{aligned} \hat{T}(\mathbf{k}, t) &= \left(\mathbf{I} - \frac{\mathbf{k}\mathbf{k}}{k^2} \right) : \\ & \mathcal{R} \left\{ -\sqrt{-1} \sum_{\mathbf{k}'+\mathbf{k}''=\mathbf{k}} [\mathbf{k} \cdot \hat{\mathbf{u}}(\mathbf{k}', t) \hat{\mathbf{u}}(\mathbf{k}'', t) \hat{\mathbf{u}}_*(\mathbf{k}, t)] \right\} \end{aligned} \quad (\text{C4a})$$

and

$$\begin{aligned} \hat{S}(\mathbf{k}, t) &= \left(\mathbf{I} - \frac{\mathbf{k}\mathbf{k}}{k^2} \right) : \\ & \mathcal{R} \left\{ \frac{\kappa}{\rho_0} \sqrt{-1} \sum_{\mathbf{k}'+\mathbf{k}''=\mathbf{k}} [\mathbf{k} \cdot \mathbf{k}'\mathbf{k}'' \hat{\mathbf{u}}_*(\mathbf{k}, t) \hat{\phi}(\mathbf{k}', t) \hat{\phi}(\mathbf{k}'', t)] \right\} \end{aligned} \quad (\text{C4b})$$

are the transfer rate due to nonlinear triadic interactions and the surface tension effect, respectively.

Here a hat $\hat{\cdot}$ represents a Fourier transform (the hat in the main text is dropped for simplicity), the subscript asterisk $(\cdot)_*$ represents the complex conjugate, $\mathcal{R}\{\cdot\}$ is the real part. It is well known that $\sum_{\mathbf{k}} \hat{T}(\mathbf{k}, t) = 0$.⁹⁵ However, the sum for $\hat{S}(\mathbf{k}, t)$ may not be zero, namely, $\sum_{\mathbf{k}} \hat{S}(\mathbf{k}, t) \neq 0$, because the kinetic energy could be transferred to the free energy if the interface area is increased.

2. Kinetic energy expansion in the spherical harmonics space

The standard Fourier spectrum is more suitable for analyzing HIT, in particular, the full-developed forced homogeneous isotropic two-phase flow containing many small droplets. For the problem of evolution of a spherical droplet located in decaying turbulent flow, it is a spherical

symmetric problem if we ignore the influence of periodic boundary conditions. Therefore, we may introduce a generalized Fourier analysis, namely, the spectral method on a spherical surface,^{96–99} to analyze the kinetic energy evolution.

At a given time t , the expansion of velocity on a spherical surface of radius r_0 under spherical harmonics can be written as

$$\mathbf{u}(r_0, \Omega) = \sum_{l=0}^{\infty} \sum_{m=-l}^l \tilde{\mathbf{u}}(l, m; r_0) Y_l^m(\Omega) \quad (\text{C5a})$$

with the coefficient

$$\tilde{\mathbf{u}}(l, m; r_0) = \int \mathbf{u}(r_0, \Omega) Y_{l*}^m(\Omega) d\Omega, \quad (\text{C5b})$$

where Ω is the solid angle, $Y_l^m(\Omega)$ ($l = 0, 1, 2, \dots; m = 0, \pm 1, \pm 2, \dots, \pm l$) denotes the well-known spherical harmonics function of degree l and order m .^{96–99} The average kinetic energy on the spherical surface of radius r_0 is

$$\begin{aligned} K(r_0) &= \frac{1}{2} \frac{\int |\mathbf{u}(r_0, \Omega)|^2 d\Omega}{\int d\Omega} \\ &= \frac{1}{8\pi} \sum_{l=0}^{\infty} \sum_{m=-l}^l \tilde{\mathbf{u}}_*(l, m; r_0) \cdot \tilde{\mathbf{u}}(l, m; r_0) \\ &= \sum_{l=0}^{\infty} \hat{E}(l; r_0), \end{aligned} \quad (\text{C6})$$

where $\hat{E}(l; r_0) = \sum_{m=-l}^l \tilde{\mathbf{u}}_*(l, m; r_0) \cdot \tilde{\mathbf{u}}(l, m; r_0) / (8\pi)$ is the average kinetic energy of degree l on the spherical surface.

REFERENCES

- ¹E. E. Michaelides, C. T. Crowe, and J. D. Schwarzkopf, “Multiphase flow handbook,” (2016).
- ²L. Scarbolo, F. Bianco, and A. Soldati, “Coalescence and breakup of large droplets in turbulent channel flow,” *Physics of Fluids* **27**, 073302 (2015).
- ³D. L. Albernaz, M. Do-Quang, J. C. Hermanson, and G. Amberg, “Droplet deformation and heat transfer in isotropic turbulence,” *Journal of Fluid Mechanics* **820**, 61–85 (2017).
- ⁴M. E. Rosti, Z. Ge, S. S. Jain, M. S. Dodd, and L. Brandt, “Droplets in homogeneous shear turbulence,” *Journal of Fluid Mechanics* **876**, 962–984 (2019).
- ⁵S. Mukherjee, A. Safdari, O. Shardt, S. Kenjereš, and H. E. A. Van den Akker, “Droplet–turbulence interactions and quasi-equilibrium dynamics in turbulent emulsions,” *Journal of Fluid Mechanics* **878**, 221–276 (2019).

- ⁶G. Soligo, A. Roccon, and A. Soldati, “Breakage, coalescence and size distribution of surfactant-laden droplets in turbulent flow,” *Journal of Fluid Mechanics* **881**, 244–282 (2019).
- ⁷J. Lu, A. Fernández, and G. Tryggvason, “The effect of bubbles on the wall drag in a turbulent channel flow,” *Physics of Fluids* **17**, 095102 (2005).
- ⁸D. Qian, J. McLaughlin, K. Sankaranarayanan, S. Sundaresan, and K. Kontomaris, “Simulation of bubble breakup dynamics in homogeneous turbulence,” *Chemical Engineering Communications* **193**, 1038–1063 (2006).
- ⁹J. Feng and I. A. Bolotnov, “Evaluation of bubble-induced turbulence using direct numerical simulation,” *International Journal of Multiphase Flow* **93**, 92–107 (2017).
- ¹⁰S. Elghobashi, “Direct Numerical Simulation of Turbulent Flows Laden with Droplets or Bubbles,” *Annual Review of Fluid Mechanics* **51**, 217–244 (2019).
- ¹¹M. S. Dodd and A. Ferrante, “On the interaction of Taylor length scale size droplets and isotropic turbulence,” *Journal of Fluid Mechanics* **806**, 356–412 (2016).
- ¹²A. Roccon, M. De Paoli, F. Zonta, and A. Soldati, “Viscosity-modulated breakup and coalescence of large drops in bounded turbulence,” *Phys. Rev. Fluids* **2**, 083603 (2017).
- ¹³O. A. Druzhinin and S. Elghobashi, “Direct numerical simulations of bubble-laden turbulent flows using the two-fluid formulation,” *Physics of Fluids* **10**, 685–697 (1998).
- ¹⁴A. FERRANTE and S. ELGHOBASHI, “On the physical mechanisms of drag reduction in a spatially developing turbulent boundary layer laden with microbubbles,” *Journal of Fluid Mechanics* **503**, 345–355 (2004).
- ¹⁵E. Russo, J. Kuerten, C. van der Geld, and B. Geurts, “Water droplet condensation and evaporation in turbulent channel flow,” *Journal of Fluid Mechanics* **749**, 666–700 (2014).
- ¹⁶J. G. M. Kuerten and A. W. Vreman, “Effect of droplet interaction on droplet-laden turbulent channel flow,” *Physics of Fluids* **27**, 053304 (2015).
- ¹⁷V. Spandan, D. Lohse, and R. Verzicco, “Deformation and orientation statistics of neutrally buoyant sub-Kolmogorov ellipsoidal droplets in turbulent Taylor–Couette flow,” *Journal of Fluid Mechanics* **809**, 480–501 (2016).
- ¹⁸J. Derksen and H. Van Den Akker, “Multi-Scale Simulations of Stirred Liquid–Liquid Dispersions,” *Chemical Engineering Research and Design* **85**, 697–702 (2007).
- ¹⁹L. Scarbolo and A. Soldati, “Turbulence modulation across the interface of a large deformable drop,” *Journal of Turbulence* **14**, 27–43 (2013).
- ²⁰H. Liu, A. J. Valocchi, and Q. Kang, “Three-dimensional lattice Boltzmann model for immisci-

- ble two-phase flow simulations,” *Phys. Rev. E* **85**, 046309 (2012).
- ²¹H. Huang, M. C. Sukop, and X.-Y. Lu, *Multiphase Lattice Boltzmann Methods: Theory and Application* (John Wiley and Sons, 2015).
 - ²²D. Juric and G. Tryggvason, “A Front-Tracking Method for Dendritic Solidification,” *Journal of Computational Physics* **123**, 127–148 (1996).
 - ²³R. Scardovelli and S. Zaleski, “DIRECT NUMERICAL SIMULATION OF FREE-SURFACE AND INTERFACIAL FLOW,” *Annual Review of Fluid Mechanics* **31**, 567–603 (1999).
 - ²⁴N. Balcázar, O. Lehmkuhl, L. Jofre, J. Rigola, and A. Oliva, “A coupled volume-of-fluid/level-set method for simulation of two-phase flows on unstructured meshes,” *Computers and Fluids* **124**, 12–29 (2016).
 - ²⁵M. Sussman, E. Fatemi, P. Smereka, and S. Osher, “An improved level set method for incompressible two-phase flows,” *Computers and Fluids* **27**, 663–680 (1998).
 - ²⁶A. K. Gunstensen, D. H. Rothman, S. Zaleski, and G. Zanetti, “Lattice Boltzmann model of immiscible fluids,” *Phys. Rev. A* **43**, 4320–4327 (1991).
 - ²⁷X. Shan and H. Chen, “Lattice Boltzmann model for simulating flows with multiple phases and components,” *Phys. Rev. E* **47**, 1815–1819 (1993).
 - ²⁸X. Shan and H. Chen, “Simulation of nonideal gases and liquid-gas phase transitions by the lattice Boltzmann equation,” *Phys. Rev. E* **49**, 2941–2948 (1994).
 - ²⁹M. R. Swift, E. Orlandini, W. R. Osborn, and J. M. Yeomans, “Lattice Boltzmann simulations of liquid-gas and binary fluid systems,” *Phys. Rev. E* **54**, 5041–5052 (1996).
 - ³⁰S. Chen and G. D. Doolen, “LATTICE BOLTZMANN METHOD FOR FLUID FLOWS,” *Annual Review of Fluid Mechanics* **30**, 329–364 (1998).
 - ³¹H.-R. Liu, C. S. Ng, K. L. Chong, D. Lohse, and R. Verzicco, “An efficient phase-field method for turbulent multiphase flows,” *Journal of Computational Physics* **446**, 110659 (2021).
 - ³²X. He, S. Chen, and R. Zhang, “A Lattice Boltzmann Scheme for Incompressible Multiphase Flow and Its Application in Simulation of Rayleigh–Taylor Instability,” *Journal of Computational Physics* **152**, 642–663 (1999).
 - ³³P. Perlekar, L. Biferale, M. Sbragaglia, S. Srivastava, and F. Toschi, “Droplet size distribution in homogeneous isotropic turbulence,” *Physics of Fluids* **24**, 065101 (2012).
 - ³⁴J. O. Hinze, “Fundamentals of the hydrodynamic mechanism of splitting in dispersion processes,” *AIChE journal* **1**, 289–295 (1955).
 - ³⁵A. E. Komrakova, D. Eskin, and J. Derksen, “Numerical study of turbulent liquid-liquid disper-

- sions,” *AIChE Journal* **61**, 2618–2633 (2015).
- ³⁶C. Shao, K. Luo, Y. Yang, and J. Fan, “Direct numerical simulation of droplet breakup in homogeneous isotropic turbulence: The effect of the Weber number,” *International Journal of Multiphase Flow* **107**, 263–274 (2018).
- ³⁷M. S. Dodd and L. Jofre, “Small-scale flow topologies in decaying isotropic turbulence laden with finite-size droplets,” *Phys. Rev. Fluids* **4**, 064303 (2019).
- ³⁸Z. Guo, K. Xu, and R. Wang, “Discrete unified gas kinetic scheme for all Knudsen number flows: Low-speed isothermal case,” *Phys. Rev. E* **88**, 033305 (2013).
- ³⁹Z. Guo, R. Wang, and K. Xu, “Discrete unified gas kinetic scheme for all Knudsen number flows. II. Thermal compressible case,” *Phys. Rev. E* **91**, 033313 (2015).
- ⁴⁰C. K. Aidun and J. R. Clausen, “Lattice-Boltzmann Method for Complex Flows,” *Annual Review of Fluid Mechanics* **42**, 439–472 (2010).
- ⁴¹K. Xu and J.-C. Huang, “A unified gas-kinetic scheme for continuum and rarefied flows,” *Journal of Computational Physics* **229**, 7747–7764 (2010).
- ⁴²P. Wang, L.-P. Wang, and Z. Guo, “Comparison of the lattice Boltzmann equation and discrete unified gas-kinetic scheme methods for direct numerical simulation of decaying turbulent flows,” *Phys. Rev. E* **94**, 043304 (2016).
- ⁴³Y. T. Bo, P. Wang, Z. L. Guo, and L.-P. Wang, “DUGKS simulations of three-dimensional Taylor-Green vortex flow and turbulent channel flow,” *Computers and Fluids* **155**, 9–21 (2017), iCMMES2015.
- ⁴⁴D. M. Anderson, G. B. McFadden, and A. A. Wheeler, “DIFFUSE-INTERFACE METHODS IN FLUID MECHANICS,” *Annual Review of Fluid Mechanics* **30**, 139–165 (1998).
- ⁴⁵C. Zhang, K. Yang, and Z. Guo, “A discrete unified gas-kinetic scheme for immiscible two-phase flows,” *International Journal of Heat and Mass Transfer* **126**, 1326–1336 (2018).
- ⁴⁶T. Chen, V. Chéron, Z. Guo, J. C. B. de Motta, T. Menard, and L.-P. Wang, “Simulation of immiscible two-phase flows based on a kinetic diffuse interface approach,” in *International Conference on Multiphase Flow* (2019).
- ⁴⁷H. Liang, B. C. Shi, Z. L. Guo, and Z. H. Chai, “Phase-field-based multiple-relaxation-time lattice Boltzmann model for incompressible multiphase flows,” *Phys. Rev. E* **89**, 053320 (2014).
- ⁴⁸J. M. Church, Z. Guo, P. K. Jimack, A. Madzvamuse, K. Promislow, B. Wetton, S. M. Wise, and F. Yang, “High accuracy benchmark problems for Allen-Cahn and Cahn-Hilliard dynamics,” *Communications in Computational Physics* **26**, 947–972 (2019).

- ⁴⁹T. Zhang, J. Wu, and X. Lin, “An interface-compressed diffuse interface method and its application for multiphase flows,” *Physics of Fluids* **31**, 122102 (2019).
- ⁵⁰J. S. Rowlinson and B. Widom, *Molecular Theory of Capillarity* (1989).
- ⁵¹C. Liu and J. Shen, “A phase field model for the mixture of two incompressible fluids and its approximation by a Fourier-spectral method,” *Physica D: Nonlinear Phenomena* **179**, 211–228 (2003).
- ⁵²D. Jacqmin, “An energy approach to the continuum surface tension method,” in *34th Aerospace sciences meeting and exhibit* (1996) p. 858.
- ⁵³P. YUE, J. J. FENG, C. LIU, and J. SHEN, “A diffuse-interface method for simulating two-phase flows of complex fluids,” *Journal of Fluid Mechanics* **515**, 293–317 (2004).
- ⁵⁴J. W. Cahn and J. E. Hilliard, “Free energy of a nonuniform system. I. Interfacial free energy,” *The Journal of chemical physics* **28**, 258–267 (1958).
- ⁵⁵J. W. Cahn and J. E. Hilliard, “Free energy of a nonuniform system. III. Nucleation in a two-component incompressible fluid,” *The Journal of chemical physics* **31**, 688–699 (1959).
- ⁵⁶Y. Li, J.-I. Choi, and J. Kim, “A phase-field fluid modeling and computation with interfacial profile correction term,” *Communications in Nonlinear Science and Numerical Simulation* **30**, 84–100 (2016).
- ⁵⁷M. Xu, H. Guo, and Q. Zou, “Hessian recovery based finite element methods for the Cahn-Hilliard equation,” *Journal of Computational Physics* **386**, 524–540 (2019).
- ⁵⁸A. Toutant, “General and exact pressure evolution equation,” *Physics Letters A* **381**, 3739–3742 (2017).
- ⁵⁹P. L. Bhatnagar, E. P. Gross, and M. Krook, “A model for collision processes in gases,” *Phys. Rev.* **94**, 511–525 (1954).
- ⁶⁰S. Chapman and T. G. Cowling, *The Mathematical Theory of Non-Uniform Gases* (Cambridge University Press, 1970).
- ⁶¹T. Chen, X. Wen, L.-P. Wang, Z. Guo, J. Wang, and S. Chen, “Simulation of three-dimensional compressible decaying isotropic turbulence using a redesigned discrete unified gas kinetic scheme,” *Physics of Fluids* **32**, 125104 (2020).
- ⁶²Y. Q. Zu and S. He, “Phase-field-based lattice Boltzmann model for incompressible binary fluid systems with density and viscosity contrasts,” *Phys. Rev. E* **87**, 043301 (2013).
- ⁶³C. Zhang, Z. Guo, and Y. Li, “A fractional step lattice Boltzmann model for two-phase flow with large density differences,” *International Journal of Heat and Mass Transfer* **138**, 1128–1141

- (2019).
- ⁶⁴P. Yue, C. Zhou, and J. J. Feng, “Spontaneous shrinkage of drops and mass conservation in phase-field simulations,” *Journal of Computational Physics* **223**, 1–9 (2007).
 - ⁶⁵L. Zheng, T. Lee, Z. Guo, and D. Rumschitzki, “Shrinkage of bubbles and drops in the lattice Boltzmann equation method for nonideal gases,” *Phys. Rev. E* **89**, 033302 (2014).
 - ⁶⁶C. Zhang and Z. Guo, “Spontaneous shrinkage of droplet on a wetting surface in the phase-field model,” *Phys. Rev. E* **100**, 061302 (2019).
 - ⁶⁷T. Lee and P. F. Fischer, “Eliminating parasitic currents in the lattice boltzmann equation method for nonideal gases,” *Phys. Rev. E* **74**, 046709 (2006).
 - ⁶⁸H. Zheng, C. Shu, and Y. Chew, “A lattice Boltzmann model for multiphase flows with large density ratio,” *Journal of Computational Physics* **218**, 353–371 (2006).
 - ⁶⁹C. M. Pooley and K. Furtado, “Eliminating spurious velocities in the free-energy lattice Boltzmann method,” *Phys. Rev. E* **77**, 046702 (2008).
 - ⁷⁰R. Van der Sman and S. Van der Graaf, “Emulsion droplet deformation and breakup with lattice Boltzmann model,” *Computer Physics Communications* **178**, 492–504 (2008).
 - ⁷¹Z. Guo, C. Zheng, and B. Shi, “Force imbalance in lattice Boltzmann equation for two-phase flows,” *Phys. Rev. E* **83**, 036707 (2011).
 - ⁷²C. Peng, L. F. Ayala, O. M. Ayala, and L.-P. Wang, “Isotropy and spurious currents in pseudopotential multiphase lattice Boltzmann models,” *Computers and Fluids* **191**, 104257 (2019).
 - ⁷³Y. Hu, D. Li, and Q. He, “Generalized conservative phase field model and its lattice Boltzmann scheme for multicomponent multiphase flows,” *International Journal of Multiphase Flow* **132**, 103432 (2020).
 - ⁷⁴C. Rosales and C. Meneveau, “Linear forcing in numerical simulations of isotropic turbulence: Physical space implementations and convergence properties,” *Physics of fluids* **17**, 095106 (2005).
 - ⁷⁵B. Duret, G. Luret, J. Reveillon, T. Ménard, A. Berlemont, and F.-X. Demoulin, “DNS analysis of turbulent mixing in two-phase flows,” *International Journal of Multiphase Flow* **40**, 93–105 (2012).
 - ⁷⁶T. Ménard, S. Tanguy, and A. Berlemont, “Coupling level set/VOF/ghost fluid methods: Validation and application to 3D simulation of the primary break-up of a liquid jet,” *International Journal of Multiphase Flow* **33**, 510–524 (2007).
 - ⁷⁷Y. Peng, W. Liao, L.-S. Luo, and L.-P. Wang, “Comparison of the lattice Boltzmann and pseudo-

- spectral methods for decaying turbulence: Low-order statistics,” *Computers and Fluids* **39**, 568–591 (2010).
- ⁷⁸C. Canuto, M. Y. Hussaini, A. Quarteroni, and T. A. Zang, *Spectral Methods: Fundamentals in Single Domains* (Springer, 2007).
- ⁷⁹A. Pothérat and K. Kornet, “The decay of wall-bounded MHD turbulence at low Rm ,” *Journal of Fluid Mechanics* **783**, 605–636 (2015).
- ⁸⁰L.-P. Wang and M. R. Maxey, “Settling velocity and concentration distribution of heavy particles in homogeneous isotropic turbulence,” *Journal of Fluid Mechanics* **256**, 27–68 (1993).
- ⁸¹R. Antonia, S. Tang, L. Djenidi, and L. Danaila, “Boundedness of the velocity derivative skewness in various turbulent flows,” *Journal of Fluid Mechanics* **781**, 727–744 (2015).
- ⁸²P. Clay, “The mechanism of emulsion formation in turbulent flow,” *Proceedings of the Section of Sciences* **43**, 852–965 (1940).
- ⁸³M. Huang and A. Leonard, “Power-law decay of homogeneous turbulence at low Reynolds numbers,” *Physics of Fluids* **6**, 3765–3775 (1994).
- ⁸⁴R. Samtaney, D. I. Pullin, and B. Kosović, “Direct numerical simulation of decaying compressible turbulence and shocklet statistics,” *Physics of Fluids* **13**, 1415–1430 (2001).
- ⁸⁵F. LUCCI, A. FERRANTE, and S. ELGHOBASHI, “Modulation of isotropic turbulence by particles of Taylor length-scale size,” *Journal of Fluid Mechanics* **650**, 5–55 (2010).
- ⁸⁶M. Lance and J. Bataille, “Turbulence in the liquid phase of a uniform bubbly air–water flow,” *Journal of Fluid Mechanics* **222**, 95–118 (1991).
- ⁸⁷B. BUNNER and G. TRYGGVASON, “Dynamics of homogeneous bubbly flows Part 2. Velocity fluctuations,” *Journal of Fluid Mechanics* **466**, 53–84 (2002).
- ⁸⁸P. Trontin, S. Vincent, J. Estivalezes, and J. Caltagirone, “Direct numerical simulation of a freely decaying turbulent interfacial flow,” *International Journal of Multiphase Flow* **36**, 891–907 (2010).
- ⁸⁹R. Canu, S. Puggelli, M. Essadki, B. Duret, T. Menard, M. Massot, J. Reveillon, and F. Demoulin, “Where does the droplet size distribution come from?” *International Journal of Multiphase Flow* **107**, 230–245 (2018).
- ⁹⁰V. Chéron, J. B. de Motta, G. Vaudor, T. Ménard, and A. Berlemont, “From droplets to particles: Transformation criteria,” in *ILASS-Europe 2019, 29th Conference on Liquid Atomization and Spray Systems* (2019).
- ⁹¹Z. Yang, C. Zhong, and C. Zhuo, “Phase-field method based on discrete unified gas-kinetic

- scheme for large-density-ratio two-phase flows,” *Phys. Rev. E* **99**, 043302 (2019).
- ⁹²Z. Yang, S. Liu, C. Zhuo, and C. Zhong, “Conservative multilevel discrete unified gas kinetic scheme for modeling multiphase flows with large density ratios,” *Physics of Fluids* **34**, 043316 (2022).
- ⁹³X. SHAN, X.-F. YUAN, and H. CHEN, “Kinetic theory representation of hydrodynamics: a way beyond the Navier–Stokes equation,” *Journal of Fluid Mechanics* **550**, 413–441 (2006).
- ⁹⁴T. Chen, L.-P. Wang, J. Lai, and S. Chen, “Inverse design of mesoscopic models for compressible flow using the Chapman-Enskog analysis,” *Advances in Aerodynamics* **3** (2021).
- ⁹⁵S. B. Pope, *Turbulent flows* (Cambridge university press, 2000).
- ⁹⁶M. Satoh, *Spectral method on a sphere* (Atmospheric Circulation Dynamics and General Circulation Models, 2014).
- ⁹⁷R. A. Phinney and R. Burridge, “Representation of the Elastic - Gravitational Excitation of a Spherical Earth Model by Generalized Spherical Harmonics,” *Geophysical Journal of the Royal Astronomical Society* **34**, 451–487 (1973).
- ⁹⁸S. Courty, G. Lagubeau, and T. Tixier, “Oscillating droplets by decomposition on the spherical harmonics basis,” *Phys. Rev. E* **73**, 045301 (2006).
- ⁹⁹H. Groemer, *Geometric applications of Fourier series and spherical harmonics*, Vol. 61 (Cambridge University Press, 1996).